ORIGINAL PAPER

# Genesis of Smectites associated with a Coal Seams Succession in the Neogene Orhaneli and Keles Coal Deposits (Bursa), NW Turkey

**Hülya Erkoyun · Selahattin Kadir · Tacit Külah**

**Abstract** The Bursa-Orhaneli and Keles-Harmanalan coal deposits were developed in swampy and fluvial-lacustrine environments in western Anatolia under the E–W-trending graben zone during the Neogene. The present study aimed to determine the mineralogical and geochemical properties of clays interlayering the coal seams to define the origin of clay minerals, in particular, smectite. These deposits, comprising argillaceous sediment, marl, coal seam, mudstone, organic-rich shale, and sandstone, were deposited in a lacustrine environment accompanied by volcanogenic materials. The characteristics of sediments and their parent rocks were examined using X-ray diffraction, scanning electron microscopy, energy dispersive spectroscopy, palynology, and chemical analyses. The association of abundant smectite with quartz, amphibole, accessory chlorite, and a decrease in feldspar in fluvial-lacustrine sediments compared to those in the smectite accompanied by feldspar and volcanic glass and the absence of quartz and amphibole in the pyroclastic units suggest that smectite had detrital and authigenic origins. Flaky smectite shows either detrital, irregularly outlined coating and filling pores of terrigenous sediments or in situ precipitation edging resorbed feldspar and devitrified volcanic glass. Chemical analyses of the smectite-rich fraction show montmorillonite compositions with an average structural formula of: $(Ca_{0.42}Na_{0.25}K_{0.08})(Al_{2.76} Fe_{0.47}Mg_{0.59}Ti_{0.07}Mn_{0.002})(Si_{7.65}Al_{0.35})O_{20}(OH)_4$.

The positive correlation of $Al_2O_3$ vs. $TiO_2$ and $K_2O$ vs. Rb may be related to the abundant detrital input. Feldspar and biotite were replaced by illite during diagenesis. An increase in the Ni/Co and V/(V + Ni) ratios in the altered units also suggest oxic, suboxic to anoxic conditions, under the control of a dry, warm to subtropical climate in fresh water and lakes during the Late Eocene to Middle Miocene. The slight enrichment of light rare earth elements (LREE) compared to heavy rare earth elements (HREE) with positive Eu and positive/negative Ce anomalies reflect fractional crystallization of feldspar. The $\delta^{18}O$ and $\delta D$ values of smectite and illite fractions and the wide range of $\delta^{34}S$ isotope values (–1.5 to 15‰) for pyrite and chalcopyrite associated with coal indicate a signature of both diagenetic and partial hydrothermal origin.

H. Erkoyun (✉) · S. Kadir
Department of Geological Engineering, Eskişehir Osmangazi University, TR-26040 Eskişehir, Turkey
e-mail: hlerkoyun08@gmail.com

T. Külah
Department of Geological Engineering, Kütahya Dumlupınar University, TR-43100 Kütahya, Turkey

## Introduction

Coal seam-intercalated clay layers formed during burial diagenesis of pyroclastic rocks in a swampy lacustrine

environment in San Miguel Mine, Atascosa, Texas, USA (Senkayi et al., 1987). Argillaceous units in the Miocene coal fields (Seyitömer, Tunçbilek, Soma, and Harmancık) have intercalated tuffs in northwest–west Anatolia (Çelik et al., 2021; Erkoyun et al., 2017, 2019; Karayiğit et al., 2017; Oskay et al., 2019). Smectitic bands were formed generally from altered volcanic ash layers having rhyolitic to dacitic composition in the Sydney Basin, Australia (Rivas-Sanchez et al., 1989), in Songzao, China (Zhao et al., 2012), in western Washington, USA (Bohor & Triplehorn, 1993), and Alaska, USA (Reinink-Smith, 1990). The alteration of tuffs to smectite was due possibly to the occurrence of Mg and Ca which were not flushed away fully in a closed system during diagenesis (Bohor & Triplehorn, 1993). Furthermore, detrital smectite in the fluvial-lacustrine units (organic-rich shale, mudstone, and sandstone) associated with early diagenetic coal seams had a terrigenous origin in Spain (Sáez et al., 2003) and Bulgaria (Yossifova et al., 2018).

Detrital smectite is abundant in terrigenous fluvial sediments such as organic-rich shale, sandstone, mudstone, and, locally, in tuff in the Seyitömer coal deposit (Erkoyun et al., 2017). In addition, the authigenic formation of the tonstein kaolin in the Tunçbilek coal deposit was from volcanic ash during diagenesis and was determined in detail (Erkoyun et al., 2019). No detailed study of the mode of formation of smectite in the Seyitömer and Tunçbilek coal deposits in western Anatolia has been reported.

The Orhaneli and Keles coal mines are the most important source of raw materials for heat energy, electricity, and mechanical energies in western Anatolia and have reserves of 102 million tons (Şengüler, 2004). The Neogene fluvial-lacustrine sediments include pyroclastics in the Orhaneli-Keles basins.

The Orhaneli and Keles coal mines have been studied previously for the purpose of coal prospecting (Bayraktar & Altınay, 1985; Bilgin et al., 1988; Çetin, 1985; Yiğitel et al., 1989); the studies were restricted to petrographic, mineralogical, and sedimentological characterization of coal (Çelik et al., 2021). Prior to the current study, no detailed information was available concerning the mineralogy, micromorphology and geochemistry, palynology, and formation conditions of the smectite associated with intercalated argillaceous sediments and volcanogenic units in coal seams in the Orhaneli and Keles coal mines. Thus, the purpose of the current study was to fill this gap

and unravel the mineralogical and geochemical evolutionary stages of the lacustrine deposits and the origin of the smectites. These results have also helped to understand the fluvial deposition, the paleoclimatic conditions, and the diagenetic environment for the precipitation of smectitic claystone which intercalates the coal seams in a fault-controlled system and the local influence of hydrothermal fluid.

## Geological Setting

Basement rocks of the study area comprise Mesozoic metamorphics and Upper Cretaceous ophiolitic mélange (Fig. 1). The Mesozoic metamorphic rocks are Triassic mica-schist, phyllite, metabasite, and marbles; and are overlain conformably by Triassic–Cretaceous marbles and locally recrystallized limestones (Okay et al., 1998, 2011). The Mesozoic metamorphic rocks are overlain tectonically by an Upper Cretaceous ophiolitic mélange which consists of ultramafic rocks, basalt, meta-clastics, and marbles (Sarıfakıoğlu et al., 2009; Şengüler, 2004). The basement units were intruded by Eocene Büyükorhan, Topuk, Göynükbelen, and Gürgenyayla granitoids (Başol, 2009). During the Miocene, the region was influenced by an extensional tectonic regime, dominated by normal faulting, which led to the occurrence of numerous basins controlled by a ~ N–S-trending graben system (Selim et al., 2006; Şengüler, 2004). These depression basins were filled by Miocene–Pliocene lacustrine sediments (Şengüler, 2004). The Orhaneli and Keles areas represent two different basins, which are separated by a threshold (horst) of basement rocks which occurred in the same tectonic system (Şengüler, 2004). In these basins, Miocene–Pliocene continental sediments overlie unconformably the basement rocks and Eocene granitoids (Fig. 2). Miocene sediments are composed of conglomerate, sandstone, mudstone, argillaceous sediments, marl, and organic-rich shale with coal seams, tuff/tuffite, and limestone deposited in a lacustrine environment. Lacustrine sediments have lateral and vertical transitions with Miocene volcanic and volcaniclastic units, showing an andesitic to dacitic composition. Miocene formations are overlain conformably by Pliocene continental sediments and volcano-sedimentary units. The Pliocene is represented by limestones, marls, tuff/tuffite, and has a total thickness of ~ 300 m in the Miocene units in the Keles area (Figs. 1 and 2;

<span style="float:right">⚪ Springer</span>
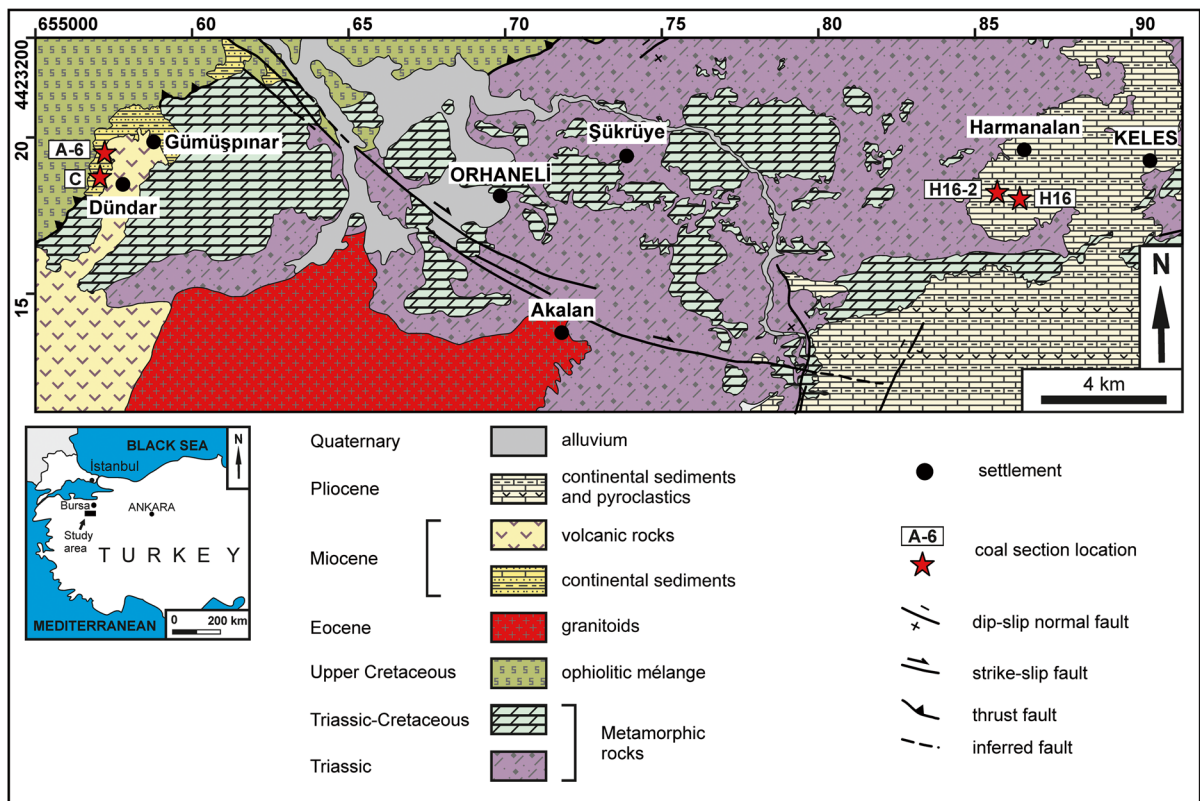
**Fig. 1** Location and geological maps of the coal-bearing Orhaneli-Gümüşpınar and Keles-Harmanalan basins and sample locations (Konak, 2002; Özaksoy et al., 2018)

Şengüler, 2004). All the aforementioned units are overlain unconformably by Quaternary alluvium.

## Description of Coal-bearing Sections

Orhaneli-Gümüşpınar Region

**A6 section** This section begins with greenish-gray colored, locally coarse sand-fine gravel bearing argillaceous sediment and continues upward with a dark brown, fractured, and friable coal seam (Figs. 3 and 4a). The coal seam in this section is 8 m thick and contains 15 cm-thick layers of marl. The coal seam is overlain by a 40 m-thick, greenish-gray, plastic, conchoidally fractured, argillaceous sediment which contains pyrite crystals (Fig. 4b) and 1–2 m-thick dark brown, organic-rich shale levels. The middle part of this section is intercalated with 1 m thick conglomerate and 4 m thick sandstone, respectively. This section continues upward

with light brown, thick-bedded (~1 m) mudstone, and beige tuff that is composed of biotite and quartz crystals, and pumice fragments. This section is overlain by beige, 10 m thick tuff that is intercalated with gray, thin-bedded (20–30 cm) marl.

**C section** The lowermost part of this section is composed of dark brown, 4 m-thick, organic-rich shale, and continues upward with 16 m-thick, argillaceous sediments and organic-rich shale levels (Fig. 3). The argillaceous sediments are exposed in two levels, generally showing a gray color, a plastic character, and are thin-bedded (20–30 cm). Dark brown 4 m-thick, organic-rich shale occurs between the two levels of argillaceous sediment. This section continues upward with volcano-sedimentary units (tuff, tuffite), mudstone, and argillaceous sediment levels intercalating sandstone. The tuff is observed in two levels. The tuffite is gray in color, bearing rounded to subrounded lithic fragments, and observed in two levels and both are 1–2 m thick. The mudstone

| ERATHEM | SYSTEM | SERIES | UNITS | LITHOLOGY | DESCRIPTION |
|---|---|---|---|---|---|
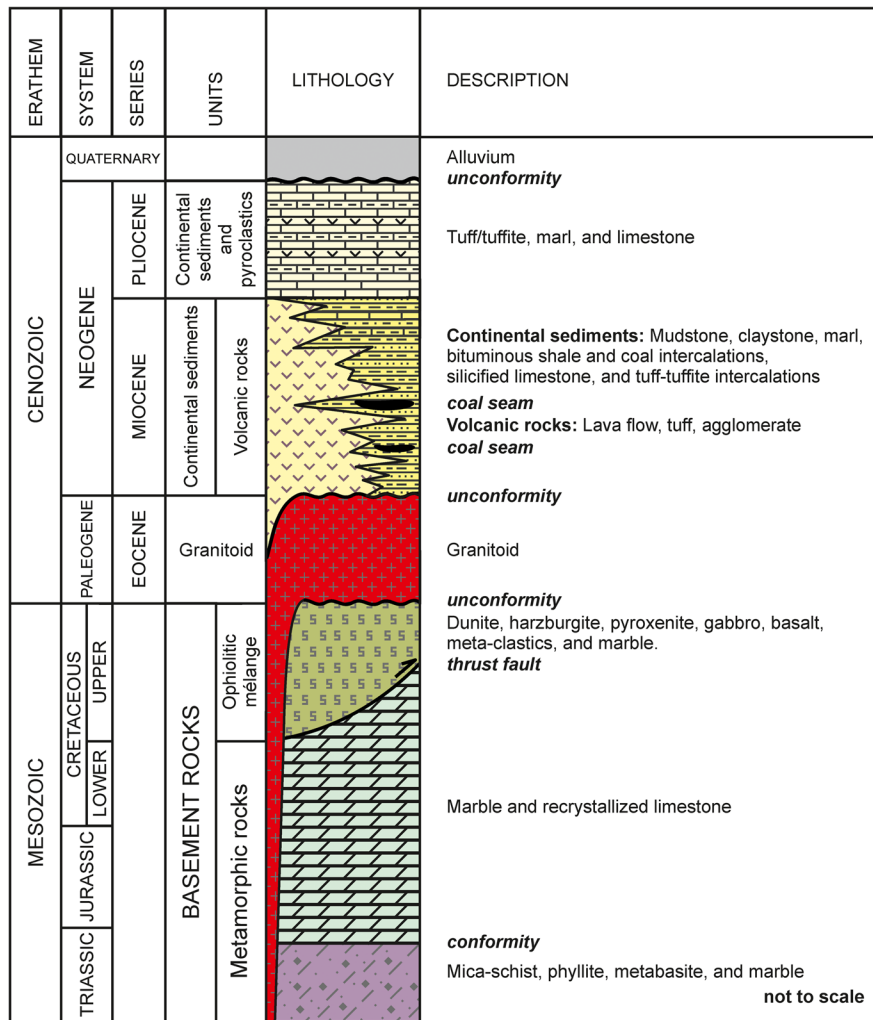


**Fig. 2** Stratigraphic section of the study area (modified from Okay et al., 1998)

shows a greenish-beige color and conchoidal fracture and is rich in organic material. The sandstone is gray in color, is thin-bedded and is 4 m thick. These units continue upward with gray marl (50 cm) and beige, thick-bedded tuff (2–3 m) with a total thickness of 30 m. The marl contains leaf fossils (Fig. 4c).

Keles-Harmanalan Region

**H16 section** This section begins with a 12 m thick, gray, hard silica level intercalated with mudstone (1.5 m thick) and dark gray, plastic, muscovite-bearing argillaceous sediments (2 m thick), and beige organic-rich shale (Fig. 3). The silica level is overlain by a 10 m thick tuff. The section continues upward with an organic-rich shale that intercalated two coal seams 2 m thick, dark gray argillaceous sediment; and light brown organic-rich shale (2 m thick) (Fig. 4d). The uppermost part of this section consists of a 50 cm-thick sandstone and is covered by a 10 m thick, greenish-gray argillaceous sediment.

**H16-2 section** The H16-2 section begins with gray, thin-bedded (10–15 cm) sandstone and continues upward with 50 cm-thick, brown argillaceous sediments and a 2 m-thick conglomerate (Fig. 3). Gray, friable, and mica-bearing tuffite overlies the
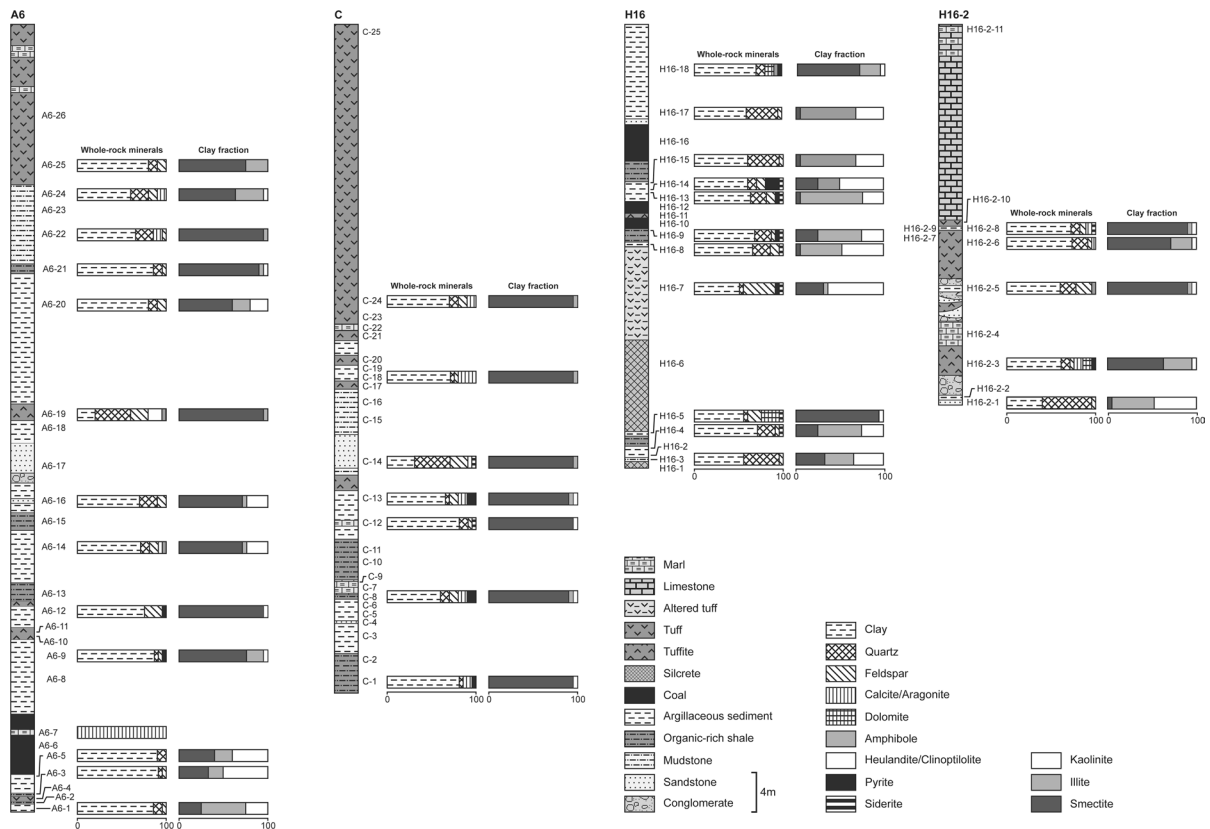
**Fig. 3** Graphical log of the Orhaneli-Gümüşpınar (A-6 and C) and Keles-Harmanalan (H16 and H16-2) basins, and the abundance of clay fraction and whole-rock minerals based on XRD results

conglomerate (Fig. 4e). The section continues upward with a 2 m-thick limestone and fluvial sediments consisting of cross-bedded conglomerate, sandstone, and tuffite and has a total thickness of 4 m. Fluvial sediments are overlain by beige, conchoidally fractured, thick-bedded argillaceous sediment (50 cm), 7 m-thick Fe-oxidized and altered tuff at the upper levels in addition, 20 m-thick, white, thin-bedded, (15–20 cm) limestone intercalates marl in the uppermost part (total thickness of 6.5 m) (Fig. 4f).

## Materials and Methods

### Sample Collection

To identify the lateral and vertical distribution of smectite in the Neogene Orhaneli-Gümüşpınar and Keles-Harmanalan coal mines, 70 samples were

collected throughout the measured sections referred to as A6, C, H16, and H16-2 (Fig. 3).

### Analytical Methods

The mineralogy was determined using optical microscopy, X-ray powder diffraction (XRD), and scanning electron microscopy – energy dispersive X-ray analysis (SEM–EDX). The rhyolitic tuff and andesitic tuffite, sandstone, organic-rich sandstone, and organic-rich shale samples were examined under a polarizing microscope (Nikon-LV 100Pol, Nikon Corporation, Tokyo, Japan). The powder XRD analysis of the parent rocks (tuff/tuffite, organic-rich shale, mudstone, sandstone), marl, and argillaceous sediments was carried out at the General Directorate of Mineral Research and Exploration of Turkey using a Rigaku D/Max–2200 instrument (Ultima PC, Tokyo, Japan). The XRD analyses were performed using CuKα
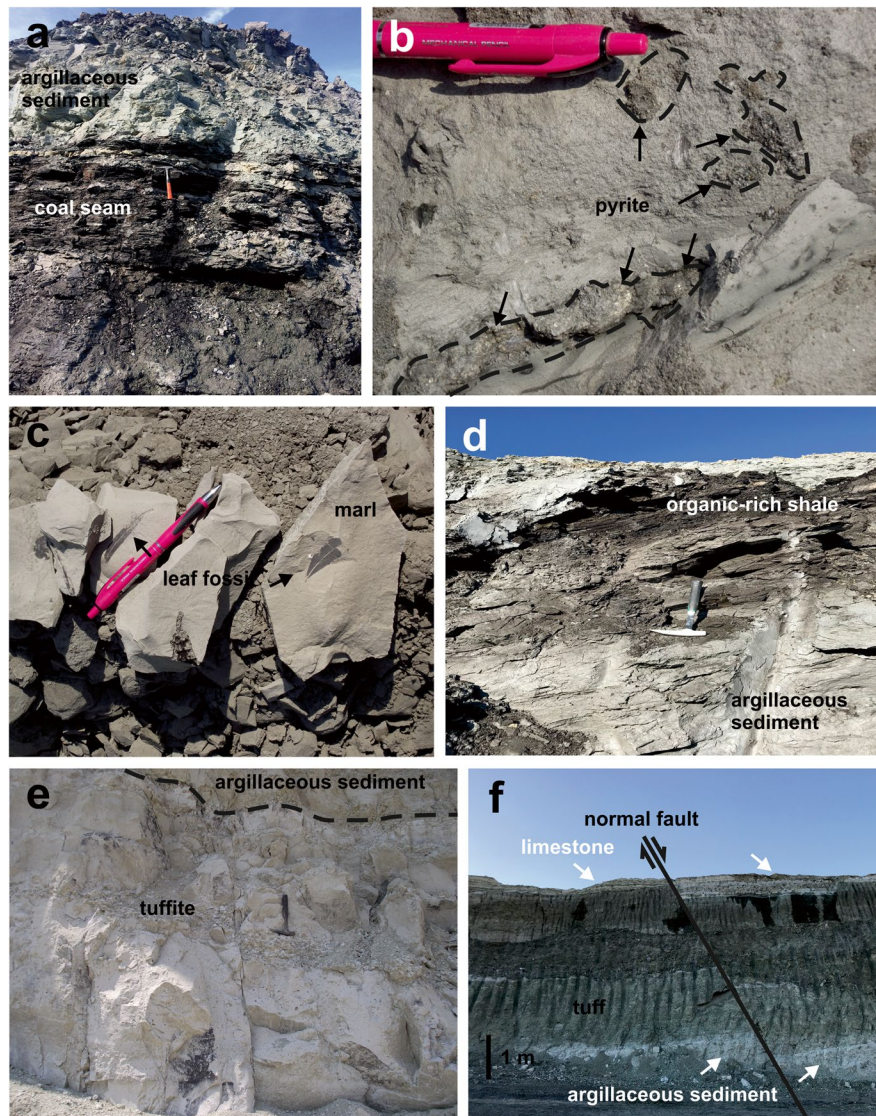
**Fig. 4** Field photographs: **a** Geometrical relationship between coal seams and argillaceous sediment in the A6 section; **b** pyrite within the organic-rich shale in the A6 section; **c** leaf fossils in the marl in the C section; **d** argillaceous sediment and organic-rich shale in the H16 section; **e** geometrical relationship between tuffite and argillaceous sediment in the H16-2 section; **f** tuff/tuffite, argillaceous sediment, marl, and fault in H16-2 section

radiation with a scanning speed of 1°2θ per min. Randomly oriented mounts of powdered whole-rock samples were scanned to determine the bulk mineralogy of each sample. Separation of the clay fraction was undertaken following the removal of free iron oxides and organic matter using the sodium dithionite-citrate procedure and hydrogen peroxide (30%) treatment, respectively (Kunze & Dixon, 1986). Carbonate was removed using acetic acid with sodium acetate buffer of pH 5 (Jackson, 1956). The treated samples for clay mineralogical analysis (<2 μm) were prepared by separating the clay fraction using sedimentation and centrifuging the suspension after an overnight dispersion in distilled water using a Hettich 32A centrifuge (Andreas Hettich GmbH and Co. KG, Tuttlingen, Germany). The clay particles were dispersed using ultrasonic vibration for ~15 min. Oriented specimens of the <2 μm fractions were prepared from each sample using the following procedure: drying with air, solvating with ethylene glycol at 60°C for 2 h, and heated

at 550°C for 2 h. Semi-quantitative abundances of rock-forming minerals were obtained using Brindley's (1980) external standard method. The relative abundances of clay-mineral fractions were determined using their basal reflections and the mineral intensity factors of Moore and Reynolds (1989).

The SEM–EDX studies were performed at the Eskişehir Osmangazi University (Turkey) using a Hitachi-Regulus 8230 FE–SEM instrument (Hitachi High-Tech, Tokyo, Japan) and an ULTIM EXTREME detector (Oxford Instruments, Abingdon, UK). Clay-dominated bulk specimens were prepared for SEM–EDX analysis by adhering the fresh broken surface of each rock sample onto an aluminum sample holder with double-sided tape. The samples were then coated with a thin film (~3 nm) of gold/palladium using a Leica EM ACE600 (Leica Microsystems, Wetzlar, Germany).

A total of seven organic-rich shales and their inter-calated coal seams were prepared according to standard palynological methods (Durand & Nicaise, 1980; Tissot & Welte, 1984) at the Turkish Petroleum Corporation (TPAO) Research Center. Relative abundances of the palynomorphs have been calculated based on at least 200 counts for each sample. Abbreviations used for different relative abundances and the corresponding number of counts are as follows: Super Abundant (S): >100 specimens (50% or more), abundant (A): between 20 and 100 specimens (10–50%), common (C): between 6 and 20 specimens (3–10%), rare (R): between 2 and 5 specimens (1–3%), present (P): only 1 specimen (0.5%). Digital images of palynomorphs were captured using a Leica DC200 digital camera system.

Chemical analyses of 23 organic-rich shale, argillaceous sediments, mudstone, sandstone, marl, and their tuff/tuffite parent rock samples were performed at the Bureau Veritas Mineral Laboratories (Vancouver, Canada) using a PerkinElmer Elan 9000 instrument (PerkinElmer, Inc., Waltham, Massachusetts, USA) inductively coupled plasma–atomic emission spectroscopy (ICP–AES) for major and trace elements and inductively coupled plasma–mass spectrometry (ICP–MS) for rare-earth elements (REE) and a Spectro (Spectro Analytical Instruments Inc., Mahwah, New Jersey, USA) XLAB–2000 PEDX–ray fluorescence spectrometer (PEDXRF). The detection limits for the analyses were between 0.01 and 0.1 wt.% for major elements, 0.1 and 5 ppm for trace elements, and 0.01 to 0.5 ppm for REE. The Eu values are correct from ICP–MS laboratories because the Ba/Eu ratio <1000 in

organic-rich shale, argillaceous sediments, mudstone, sandstone, marl, and tuff/tuffite samples (except H16-14 and C-14) (Loges et al., 2012).

The chemical index of weathering (CIW) of organic-rich shale, argillaceous sediments, mudstone, sandstone, marl, and tuff/tuffite whole-rock samples was calculated using the following equation (Harnois, 1988):

$$CIW = [Al_2O_3/(Al_2O_3 + CaO^* + Na_2O)] \times 100$$

where $CaO^* =$ The CaO content incorporated in the silicate fraction.

Nine smectite and illite clay fractions were purified and analyzed for the H and O stable isotopes in the Cornell Isotope Laboratory at Cornell University, New York. Separation was undertaken after the removal of free iron oxides and organic matter using the sodium dithionite-citrate procedure and hydrogen peroxide (30%) treatments as described by Kunze and Dixon (1986). The isotope corrections were performed using a two-point normalization (regression) based on international standards (IAEA CO–1 and IAEA CO–8) for $\delta^{18}O$ and CH–7 and benzoic acid for $\delta D$. The analyses were performed using a Thermo Delta V (Thermo Fisher Scientific, Waltham, MA, USA) isotope ratio mass spectrometer interfaced with a temperature-conversion elemental analyzer. The delta values for $^2H$ and $^{18}O$ were measured against the primary reference scale of Clayton and Mayeda (1963). The data are reported in standard delta notation as per mil deviations from V-SMOW (Vienna Standard Mean Ocean Water). The standard deviation for internal standard benzoic acid for $\delta^{18}O$ is 1.01% and for $\delta D$ is 1.24%.

The $\delta^{34}S$ was determined on five pyrite and chalcopyrite samples which were selected by handpicking under a binocular microscope. Stable-isotope analysis ($\delta^{34}S$) was conducted at the University of Arizona Department of Geosciences using an MAT 261–8 mass spectrometer [Thermo Fisher (Finnigan Corporation), Bremen, Germany]. The results of $\delta^{34}S$ were referenced to V-CDT (Vienna Canyon Diablo Troilite).

$\delta^{34}S$ was measured on $SO_2$ gas in a continuous-flow gas-ratio mass spectrometer (ThermoQuest Finnigan Delta PlusXL, Tucson, Arizona, USA). The samples were combusted at 1030°C with $O_2$ and $V_2O_5$ using an elemental analyzer (Costech, Tucson, Arizona, USA) coupled to the mass spectrometer. Standardization was based on international

standards OGS–1 and NBS123 (Hosono et al., 2014), and several other sulfides and sulfate materials for sulfur that have been compared between laboratories. Calibration was linear in the range –10 to + 30%. Precision was estimated to be –0.15% or better (1 s) based on repeated internal standards.

## Results

Petrography

The argillaceous volcano-sedimentary parent rocks of the coal mines were determined as rhyolitic tuff and andesitic tuffite, sandstone, organic-rich sandstone, and organic-rich shale. The rhyolitic tuff exhibits porphyritic and broken porcelain texture and is composed of partially altered and seriticized sanidine with Fe (oxyhydr)oxide character, a small amount of plagioclase (oligoclase), partially to completely argillized muscovite, and partially oxidized biotite and quartz in an argillized and carbonaceous groundmass (Fig. 5a). Muscovite and biotite crystals are bent. Quartz crystals have an irregular morphology and sharp edges. Volcanic glass and irregular pumice materials are abundant in rhyolitic tuff (Fig. 5a). Andesitic tuffite is composed of partially argillized plagioclase, a small amount of sanidine and pyroxene, partially-to-completely oxidized biotite, metamorphic, ophiolitic, and quartzite rock fragments, cemented by argillized and Fe (oxyhydr) oxidized groundmass (Fig. 5b–c). The amount of tuff/tuffite increases toward the Orhaneli-Gümüşpınar region.

Sandstone comprises monocrystalline and polycrystalline quartz, partially argillized bent muscovite, chloritized bent biotite, partially sericitized plagioclase, orthoclase, serpentinite rock fragments, and zeolite cemented by clay (Fig. 5d–f). Organic-rich sandstone was composed of abundant anhedral quartz, chloritized bent biotite, argillized feldspars, and brownish-black organic matter showing thin lamellae (Fig. 5g). Organic-rich shale consisted of argillized and sericitized brownish-black organic matter in a thin layer parallel to the lamination, cristobalite veins, and opaque minerals (Fig. 5h). The amount of fluvial sediments increased toward the Keles-Harmanalan region.

### Mineralogical Composition

**Orhaneli-Gümüşpınar region, A6 section** Smectite is a major constituent in clay-fraction and whole-rock samples, associated with small amounts of kaolinite and illite in the A6 section of the Orhaneli-Gümüşpınar region (Table 1 and Figs. 3 and 6). Abundant quartz, aragonite/calcite, feldspar, heulandite/clinoptilolite, and dolomite, are accompanied by accessory pyrite, siderite, and amphibole in organic-rich shale, argillaceous sediment, sandstone, tuff/tuffite, and mudstone. Smectite is found in tuff/tuffite, organic-rich shale, argillaceous sediment, sandstone, and mudstone, and in notable amounts in sandstone above and below the coal seams. Kaolinite occurs in organic-rich shale, and argillaceous sediments and illite is found in organic-rich shale, argillaceous sediments mudstone, and tuff.

**Orhaneli-Gümüşpınar region, C section** Smectite is the main clay mineral and it occurs in organic-rich shale, argillaceous sandstone, and tuff (Table 1 and Fig. 3). The intensity of smectite decreased toward the sandstone and tuff. The kaolinite and illite exist as accessory minerals and in smaller amounts than those in the A6 section. Feldspar, quartz, aragonite/calcite, pyrite, and siderite were detected in organic-rich shale, marl, and tuff.

**Keles-Harmanalan region, H16 section** Abundant smectite and occasionally kaolinite and small amounts of illite were determined in the Keles-Harmanalan region (Table 1). The concentration of smectite in the H16 and H16-2 sections of the Keles-Harmanalan region was less than that observed in the Orhaneli-Gümüşpınar region (Fig. 3). Smectite, illite, and kaolinite were associated with quartz, feldspar, and accessory pyrite, siderite, and amphibole in mudstone, argillaceous sediments, tuff, and organic-rich shale (Fig. 6). Smectite was found predominantly in argillaceous sediments. Illite occurs in argillaceous sediments, and organic-rich shale, and its amount decreased in sandstone, and tuff/tuffite. Kaolinite was determined in tuff, argillaceous sediments, mudstone, and organic-rich shale.

**Keles-Harmanalan region, H16-2 section** Smectite is the main clay mineral and occurs in tuff/tuffite and argillaceous sediments (Table 1). The amounts of kaolinite and illite decreased relative to the H16 section (Fig. 3). Aragonite/calcite and other non-clay minerals were detected in sandstone, tuff/tuffite and argillaceous sediments.
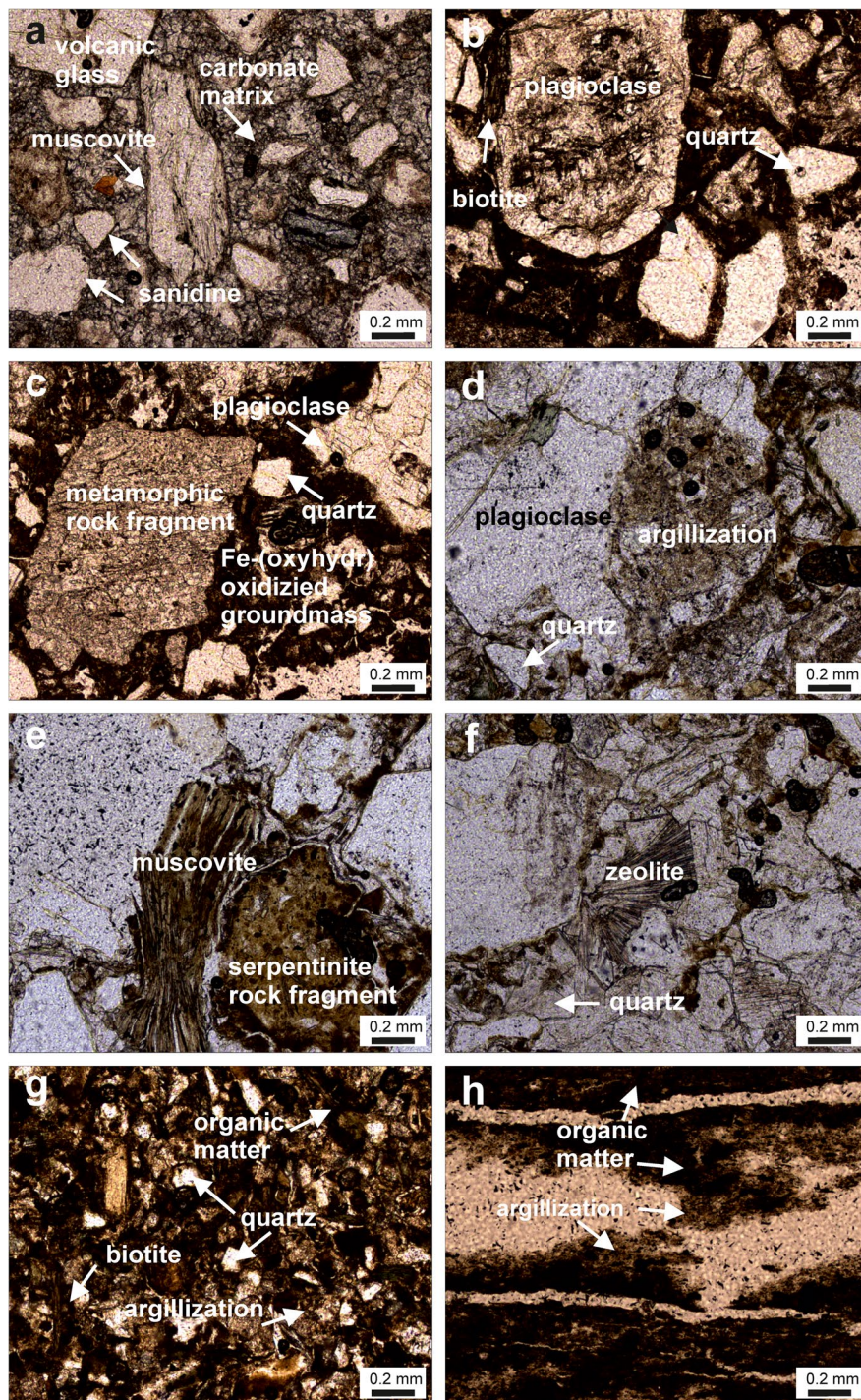
**Fig. 5** Thin-section photomicrographs of the Orhaneli-Gümüşpınar and Keles-Harmanalan host rocks: **a** partially argillized and seric-itizatied sanidine, argillized muscovite, and volcanic glass in argillized and carbonate groundmass of rhyolitic tuff (A6-25); **b–c** argil-lized plagioclase, quartz, pyroxene, biotite, and metamorphic rock fragment in Fe-(oxyhdr)oxidized groundmass of andesitic tuffite (C-20); **d–f** partially argillized bent muscovite, quartz, plagioclase, serpentinite rock fragments, and zeolite minerals in an argillized groundmass of sandstone (C-14); **g** chloritized bent biotite, anhedral quartz, and brownish-black organic matter in organic-rich sand-stone (C-15); **h** argillized and sericiticized brownish-black organic matter in thin layers parallel to laminate in organic-rich shale (A6-13)

**Table 1** Mineralogical composition of samples from the Orhaneli-Gümüşpınar and Keles-Harmanalan coal mines. Sme: smectite, Ilt/Mca: illite/mica, Kln: kaolinite, Chl: chlorite, Hul/Cpt: heulandite/clinoptilolite, Py: pyrite, Fsp: feldspar, Qz: quartz, Amp: amphibole, Arg/Cal: aragonite/calcite, Dol: dolomite, Sid: siderite, acc: accessory, +: relative abundance of mineral (mineral name abbreviations after Whitney & Evans, 2010)

| Sample | Lithology | Sme | Ilt/Mca | Kln | Chl | Hul/Cpt | Py | Fsp | Qz | Amp | Arg/Cal | Dol | Sid |
|---|---|---|---|---|---|---|---|---|---|---|---|---|---|
| | Orhaneli-Gümüşpınar | | | | | | | | | | | | |
| A6-1 | Argillaceous sediment | + | + + | + | acc | | | acc | + | | | | acc |
| A6-3 | Organic-rich shale | + + | + | + + | + | | | acc | acc | | | | |
| A6-5 | Argillaceous sediment | + + | + | + + | acc | | | acc | + | | | | acc |
| A6-7 | Marl | | | | | | | | | | + + + + + | | |
| A6-9 | Argillaceous sediment | + + + + | acc | + | + | | acc | acc | acc | | | | |
| A6-12 | Argillaceous sediment | + + + + | acc | | | | acc | + | | | | | |
| A6-14 | Argillaceous sediment | + + + | acc | + | acc | acc | | + | + | acc | | | acc |
| A6-16 | Sandstone | + + + | acc | + | | | | + | + + | | | | |
| A6-19 | Tuffite | + | acc | | | + | | + | + + | acc | | | |
| A6-20 | Argillaceous sediment | + + + | + | + | | | | + | + | | | | |
| A6-21 | Organic-rich shale | + + + + | acc | acc | | | | acc | + | | | | |
| A6-22 | Mudstone | + + + + | acc | | | | | acc | + + | | + | | |
| A6-24 | Mudstone | + + | + | acc | | | | + | + + | | + | | |
| A6-25 | Tuff | + + + | + | | | | | + | + | | | | |
| C-1 | Organic-rich shale | + + + + | | acc | | | acc | | acc | | + | | |
| C-8 | Organic-rich shale | + + + | acc | acc | | | + | + | + | | + | | |
| C-12 | Marl | + + + + | | acc | | | | acc | + | | | | acc |
| C-13 | Argillaceous sediment | + + + | acc | acc | | | + | + | acc | | + | | |
| C-14 | Sandstone | + + | acc | | | acc | | + | + + | | | | acc |
| C-18 | Argillaceous sediment | + + + + | acc | | | | | acc | acc | | + + | | |
| C-24 | Tuff | + + | acc | | | | | + | + | | + | | |
| | Keles-Harmanalan | | | | | | | | | | | | |
| H16-3 | Mudstone | + | + | + | acc | | | acc | + + | | | | |
| H16-4 | Argillaceous sediment | + | + + | + | acc | | | acc | + | | | | acc |
| H16-5 | Argillaceous sediment | + + + | | acc | acc | | | + + | acc | | | + | acc |
| H16-7 | Tuff | + | acc | + + | | | acc | + + | acc | | | | acc |
| H16-8 | Argillaceous sediment | acc | + + | + + | acc | | | + | + + | | | | acc |
| H16-9 | Organic-rich shale | + | + + | + | acc | | acc | acc | + + | | | | acc |
| H16-13 | Argillaceous sediment | acc | + + + | + | acc | | acc | + | + + | | | | acc |
| H16-14 | Argillaceous sediment | + | + | + + | acc | | + + | + | + | | | | acc |
| H16-15 | Argillaceous sediment | acc | + + | + | acc | | | acc | + + | | | | |
| H16-17 | Argillaceous sediment | acc | + + | + | acc | | | acc | + + | | | | |
| H16-18 | Argillaceous sediment | + + + | + | acc | | | acc | acc | + | acc | | + | acc |
| H16-2–1 | Sandstone | acc | + | + | | | | acc | + + + | acc | | | |
| H16-2–3 | Tuffite | + + | + | acc | | | acc | acc | + | | + | + | |
| H16-2–5 | Argillaceous sediment | + + + | acc | acc | | | | + | + | acc | | | |
| H16-2–6 | Tuff | + + + | + | acc | | | | acc | + | | acc | | |
| H16-2–8 | Argillaceous sediment | + + + | acc | acc | | | | + | + + | | + | | acc |

Smectite was identified by a broad peak at 14.18–14.90 Å which expanded to 16.90–17.48 Å following ethylene-glycol solvation; the peak collapsed to 9.92–9.96 Å following heating to 550°C (Fig. 6a–c). Kaolinite was determined by means of a narrow, sharp peak at 7.13 Å, and was not affected by ethylene–glycol
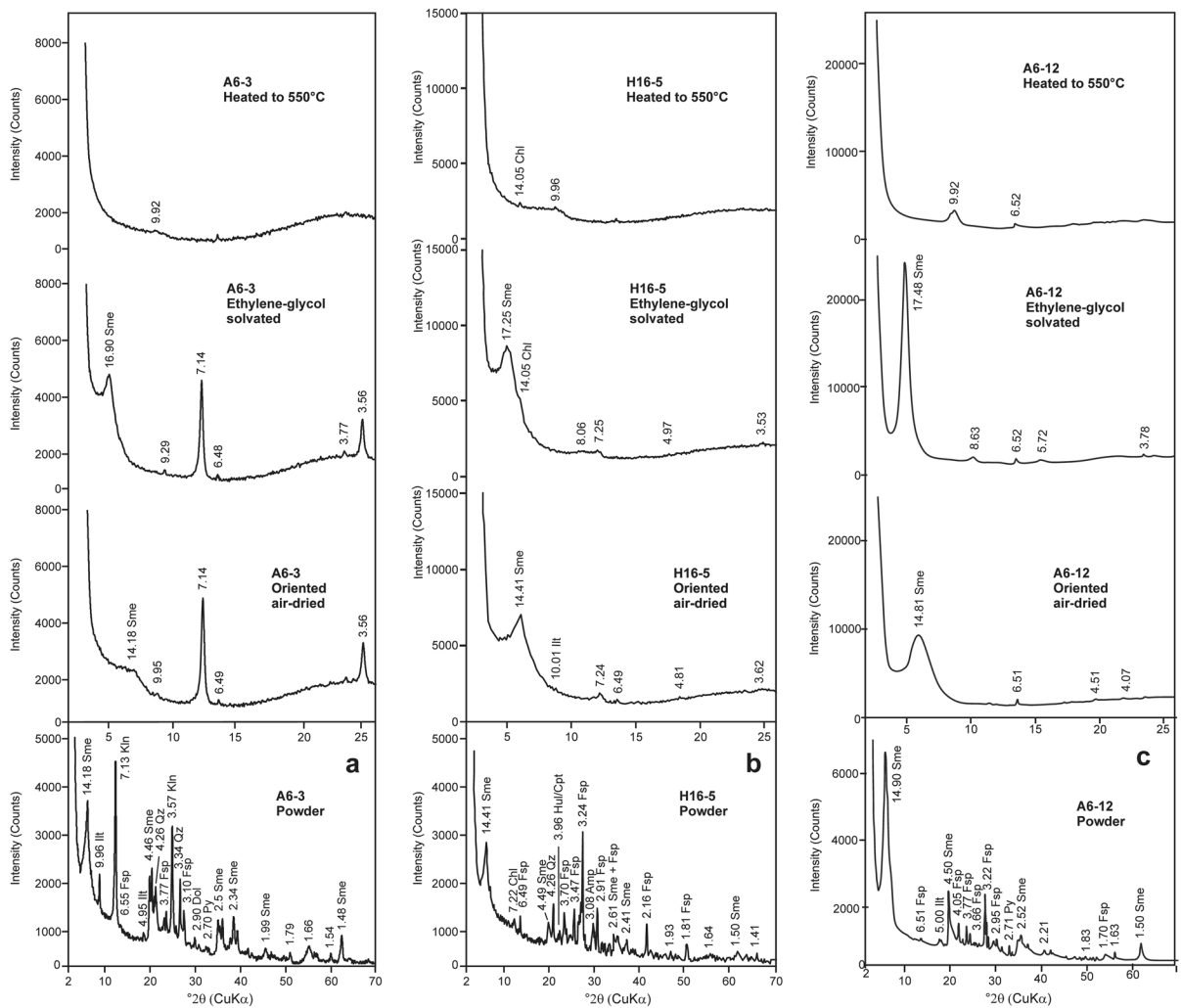
**Fig. 6** XRD patterns of the bulk smectite: **a** – abundant, **b** – detrital, and **c** – authigenic sediment samples, oriented air-dried, ethylene glycol-solvated, and heated at 550°C. Sme: smectite, Ilt: illite, Kln: kaolinite, Chl: chlorite, Hul/Cpt: heulandite/clinoptilolite, Qz: quartz, Fsp: feldspar, Amp: amphibole, Dol: dolomite, Py: pyrite

solvation; the basal (001) peaks collapsed following heating to 550°C (Fig. 6a). Illite/mica was identified by peaks at 9.96 and 4.95–5.00 Å. Feldspar was determined by peaks at 3.10–3.24, 3.70, 3.77, 4.05, and 6.49–6.55 Å. Chlorite was determined by a peak at 14.05 Å following ethylene-glycol treatment and not affected by heating at 550°C (Fig. 6b). Heulandite/clinoptilolite and pyrite were determined by peaks at 3.96 and 2.70–2.71 Å, respectively.

The SEM studies were carried out on argillaceous sediments, organic-rich shale, mudstone, and sandstone intercalating coal seams in the Bursa-Orhaneli and Keles-Harmanalan coal mines. Smectite shows two types of

morphologies: (1) platy and flaky smectite edging devitrified glass shards and highly resorbed feldspar – the latter shows bar-shaped, and subparallel comb structure in tuffaceous materials within the organic-rich shale (Fig. 7a–c); and (2) irregular flaky smectite is mostly coating the detrital volcanogenic materials or filling the pores in the fluvial sedimentary units such as mudstone and sandstone (Fig. 7d–h). Smectite crystals also edge fibrous crystals resembling illite formed via a dissolution–precipitation mechanism (Fig. 7e, f). Smectitic materials also enclose sphere-shaped opal-CT (Fig. 7g). The pores between the smectite crystals are filled locally by framboidal pyrite (Fig. 7h), aragonite crystals mostly showing radial

🖄 Springer
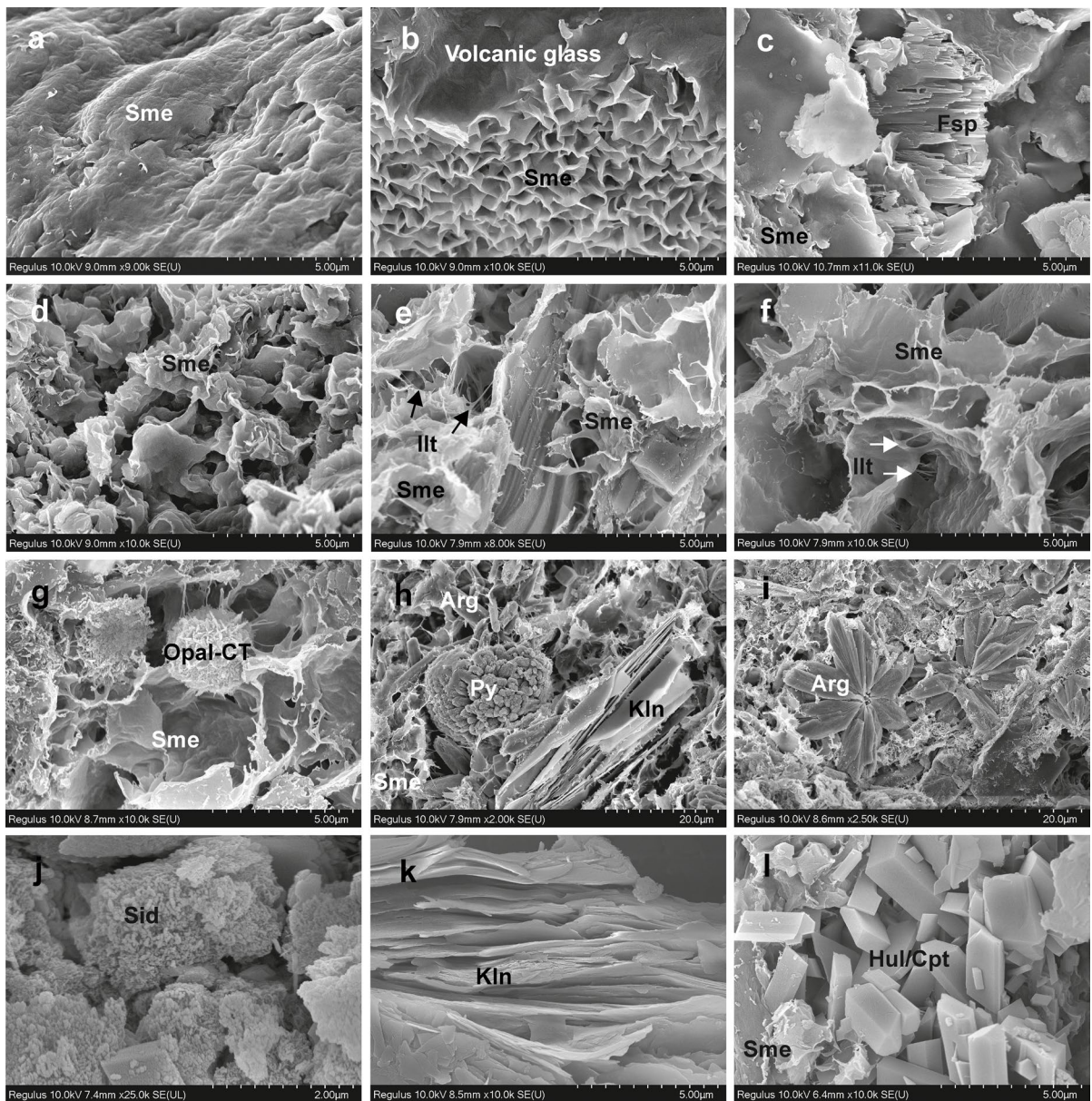
**Fig. 7** SEM images of: **a** oriented platy smectite (A6-3); **b** smectite flakes edging devitrified volcanic glass (A6-3); **c** smectite flakes edging altered feldspar (A6-9); **d–f** flaky smectite locally edging illite coating and detrital materials (H16-5; A6-3; C-8); **g** spherical opal-CT between smectite flakes (C-8); **h** framboidal pyrite filling voids among smectite associated with platy kaolinite and aragonite (H6-14); **i** radial aragonite crystal in the void of smectite flakes (C-8); **j** siderite crystals in voids of smectite (H16-14); **k** close view of book-like kaolinite (A16-4); **l** blocky, euhedral heulandite/clinoptilolite crystals (C-14)

morphology (Fig. 7i), and siderite crystals (Fig. 7j) and are associated with book-like, subparallel oriented, and anhedral kaolinite (Fig. 7k). Blocky euhedral heulandite/clinoptilolite crystals are associated with the small amount of smectite (Fig. 7l).

## Palynology

The dominant terrestrial wood-type organic matter was determined in all of the samples except C-1; light-colored amorphous type organic matter and

Springer

light-colored terrestrial (herbaceous) organic matter were identified (Fig. 8a).

Palynological analysis showed that the samples are poor in organic palynomorph content. The common palynomorphs are *Bisaccat pollen* (6–20%) in sample A6-7 (Fig. 8b). *Botryococcus braunii* is determined at a weight percentage of 6–20% in sample C-1 (Fig. 8c). Rare (2–5%) *Inaperturopollenites hiatus* was found in sample A6-3 (Fig. 8d); *Laevigatosporites sp., Leiotriletes adriennis, Subtriporopollenites simplex* and *Intratripollenites instructus* were found in the A6, C, and H16 sections.

Chemical analyses

**Major element oxides** The chemical analyses of representative organic-rich shale, argillaceous sediment, mudstone, sandstone, marl, and tuff/tuffite samples collected from the study area are presented in Table 2. The compositions of argillaceous sediments in the Orhaneli-Gümüşpınar and Keles-Harmanalan areas are characterized by small $SiO_2$ (ave. 53.53 and 49.01 wt.%) and large $Al_2O_3$ (ave. 19.07 and 16.62 wt.%) values, respectively. Tuff sample (H16-7) is composed of $SiO_2$ (51.70 wt.%) and significant amounts of $Al_2O_3$ (22.37 wt.%), $Fe_2O_3$ (4.97 wt.%), and MgO (1.20 wt.%). The $Al_2O_3/TiO_2$ ratios range between 26.1 and 143.3 in Orhaneli-Gümüşpınar and between 23.7 and 69.8 in Keles-Harmanalan.

In the $TiO_2$/Ni discrimination diagram (Fig. 9; Floyd et al., 1989) most of the argillaceous sediment samples fall mainly in the acidic magmatic rock portion, except for a few samples that fall into the sedimentary rock field.

The plot of argillaceous sediments on the $SiO_2$ vs. $Al_2O_3 + K_2O + Na_2O$ diagram shows that clay minerals formed under arid and semi-arid conditions (Fig. 10; Suttner & Dutta, 1986). The $Al_2O_3$ vs. $TiO_2$ plot ($r^2 = 0.61$) (Fig. 11a) exhibits a positive
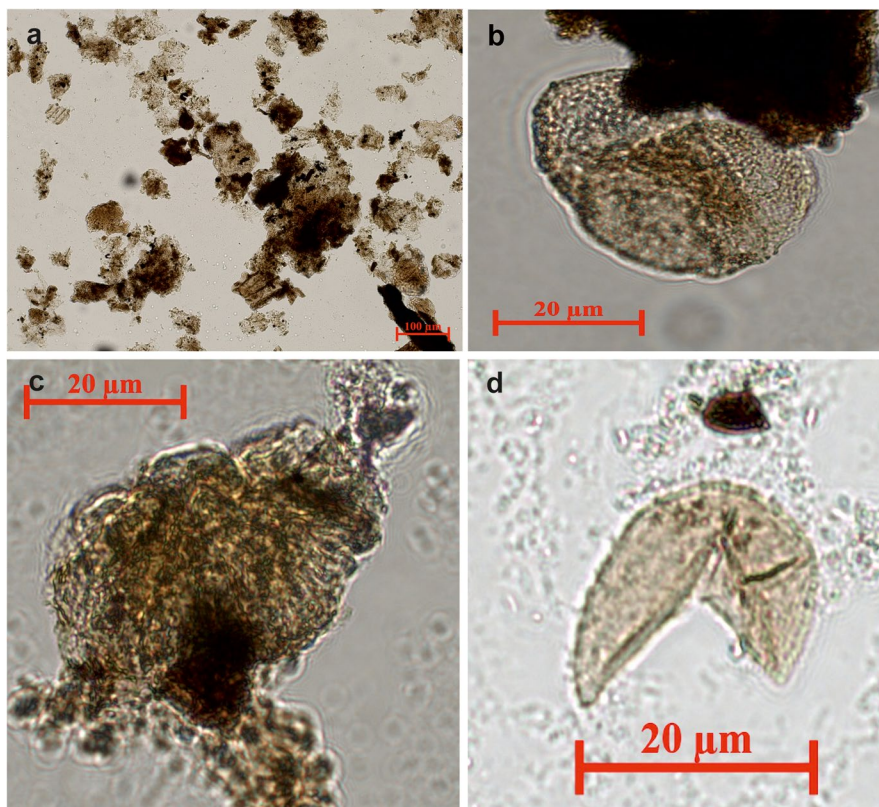


**Fig. 8** Organic matter and pollen types from Orhaneli-Gümüşpınar and Keles-Harmanalan coal mines are: **a** terrestrial organic matter (C-1); **b** *Bisaccat pollen* (A6-7); **c** *Botryococcus braunii* (C-1); **d** *Intratripollenites instructus* (A6-3)

**Table 2** Major- (wt.%) and trace-element (ppm) compositions of fresh and altered rocks from the study area (see Table 1 for the mineralogical compositions of the samples)

Orhaneli-Gümüşpınar Area

| Major oxides (wt.%) | Organic-rich shale | | | Argillaceous sediment | | | | Mudstone | Sandstone | |
|---|---|---|---|---|---|---|---|---|---|---|
| | A6-3 | A6-21 | Ave | A6-1 | A6-12 | C-13 | Ave | A6-22 | A6-16 | C-4 |
| $SiO_2$ | 41.08 | 54.52 | 47.80 | 54.67 | 53.99 | 51.94 | 53.53 | 58.46 | 65.44 | 64.46 |
| $Al_2O_3$ | 24.42 | 14.99 | 19.71 | 23.00 | 18.57 | 15.64 | 19.07 | 12.22 | 11.66 | 13.54 |
| $Fe_2O_3$ | 1.83 | 7.73 | 4.78 | 4.84 | 4.43 | 8.69 | 5.99 | 3.34 | 5.75 | 3.28 |
| MgO | 0.82 | 3.26 | 2.04 | 1.67 | 2.79 | 4.67 | 3.04 | 2.29 | 3.27 | 1.81 |
| CaO | 1.18 | 1.92 | 1.55 | 0.77 | 2.75 | 1.12 | 1.55 | 6.21 | 4.13 | 4.89 |
| $Na_2O$ | 0.13 | 0.15 | 0.14 | 0.29 | 0.92 | 0.29 | 0.50 | 0.66 | 2.16 | 2.22 |
| $K_2O$ | 0.92 | 1.70 | 1.31 | 2.83 | 0.46 | 1.40 | 1.56 | 0.88 | 1.58 | 1.44 |
| $TiO_2$ | 0.42 | 0.44 | 0.43 | 0.72 | 0.71 | 0.52 | 0.65 | 0.38 | 0.30 | 0.39 |
| $P_2O_5$ | 0.13 | 0.09 | 0.11 | 0.03 | 0.11 | 0.05 | 0.06 | 0.03 | 0.09 | 0.09 |
| MnO | 0.02 | 0.04 | 0.03 | 0.03 | 0.02 | 0.04 | 0.03 | 0.02 | 0.09 | 0.03 |
| $Cr_2O_3$ | 0.003 | 0.182 | 0.093 | 0.016 | <0.002 | 0.075 | <0.030 | 0.021 | 0.409 | 0.12 |
| TOT/S | 0.41 | <0.02 | <0.22 | 0.05 | 0.96 | 0.05 | <0.35 | <0.02 | 0.03 | 0.70 |
| TOT/C | 12.08 | 0.09 | 6.085 | 0.64 | 0.09 | 0.13 | 0.29 | 1.17 | 0.45 | 0.69 |
| LOI | 28.9 | 14.7 | 21.8 | 10.9 | 15.0 | 15.3 | 13.73 | 15.3 | 4.9 | 7.5 |
| Total | 99.91 | 99.84 | 99.88 | 99.83 | 99.85 | 99.82 | 99.83 | 99.86 | 99.84 | 99.86 |
| CIW | 91.22 | 80.27 | 85.75 | 92.59 | 74.13 | 86.19 | 84.30 | 49.68 | 51.35 | 51.96 |
| Ba | 331 | 412 | 371.5 | 662 | 439 | 295 | 465 | 291 | 444 | 511 |
| Cr | 20.5 | 1245.2 | 632.8 | 109.4 | 13.6 | 513.1 | 212.0 | 143.7 | 2798.3 | 821 |
| Co | 6.7 | 38.1 | 22.4 | 12 | 15.8 | 60.5 | 29.4 | 7.9 | 28 | 27.4 |
| Cs | 3.3 | 38.5 | 20.9 | 16.1 | 4.1 | 41.5 | 20.6 | 26 | 4.2 | 29 |
| Ga | 17.7 | 15.7 | 16.7 | 25.5 | 15.5 | 14.7 | 18.6 | 13.6 | 11 | 13.1 |
| Hf | 3.5 | 6.2 | 4.9 | 4.8 | 3.2 | 3.1 | 3.7 | 3.8 | 2.7 | 3.7 |
| Nb | 4.6 | 10.1 | 7.4 | 17 | 9.9 | 9.5 | 12.1 | 16.2 | 8.6 | 8.1 |
| Rb | 36.2 | 99.2 | 67.7 | 177.4 | 9.7 | 90.6 | 92.6 | 85.4 | 45.9 | 57.3 |
| Sn | <1 | <1 | <1 | 3 | 1 | 1 | 1.7 | 3 | <1 | 1 |
| Sr | 85.4 | 111 | 98.2 | 109.4 | 304.7 | 214.6 | 209.6 | 194.7 | 310.7 | 363.5 |
| Ta | 0.6 | 0.7 | 0.7 | 1.1 | 0.6 | 0.6 | 0.8 | 1.4 | 1 | 0.6 |
| Th | 16.5 | 9.3 | 12.9 | 21.8 | 10.6 | 13.6 | 15.3 | 17 | 9.4 | 9 |
| U | 3.5 | 1.4 | 2.5 | 5.3 | 3.1 | 1.8 | 3.4 | 3 | 0.9 | 1.9 |
| V | 36 | 60 | 48 | 131 | 111 | 66 | 102.7 | 50 | 101 | 71 |
| W | <0.5 | 2.7 | <1.6 | 4.6 | 2.5 | 5 | 4 | 1.8 | 1.5 | 1.6 |
| Zr | 140.3 | 252.4 | 196.4 | 171.8 | 113.3 | 116.5 | 133.9 | 150 | 96.3 | 145.1 |
| Y | 12.6 | 15.5 | 14.1 | 34.5 | 15.9 | 16.2 | 22.2 | 31.8 | 20.6 | 12.6 |
| La | 24.6 | 22.7 | 23.7 | 61.4 | 30.5 | 23.2 | 38.4 | 41.2 | 45.5 | 23.9 |
| Ce | 49.1 | 45.7 | 47.4 | 114.4 | 57.6 | 44.6 | 72.2 | 65.4 | 85.7 | 46.2 |
| Pr | 5.11 | 5.21 | 5.16 | 12.37 | 6.21 | 4.95 | 7.84 | 8.37 | 9.20 | 4.82 |
| Nd | 18.6 | 19.5 | 19.1 | 45.4 | 24.9 | 20 | 30.1 | 30 | 32.9 | 16.9 |
| Sm | 3.53 | 4.03 | 3.78 | 8.61 | 5.03 | 3.67 | 5.77 | 6.02 | 5.39 | 3.25 |
| Eu | 0.82 | 0.88 | 0.85 | 1.75 | 1.33 | 0.95 | 1.34 | 1.27 | 1.05 | 0.80 |
| Gd | 2.82 | 3.20 | 3.01 | 6.79 | 4.44 | 3.23 | 4.82 | 5.47 | 4.19 | 2.40 |
| Tb | 0.42 | 0.47 | 0.45 | 1.01 | 0.64 | 0.48 | 0.71 | 0.80 | 0.62 | 0.38 |
| Dy | 2.43 | 2.81 | 2.62 | 5.95 | 3.55 | 2.93 | 4.14 | 5.02 | 3.57 | 2.17 |
| Ho | 0.43 | 0.59 | 0.51 | 1.15 | 0.69 | 0.58 | 0.81 | 0.91 | 0.70 | 0.42 |

**Table 2** (continued)

| Er | 1.22 | 1.65 | 1.44 | 3.18 | 1.95 | 1.77 | 2.30 | 2.68 | 2.06 | 1.27 |
|---|---|---|---|---|---|---|---|---|---|---|
| Tm | 0.16 | 0.25 | 0.21 | 0.45 | 0.24 | 0.25 | 0.31 | 0.39 | 0.31 | 0.17 |
| Yb | 1.15 | 1.80 | 1.48 | 3.03 | 1.45 | 1.67 | 2.05 | 2.67 | 1.97 | 1.12 |
| Lu | 0.18 | 0.25 | 0.22 | 0.47 | 0.21 | 0.27 | 0.32 | 0.37 | 0.33 | 0.19 |
| Pb | 42.5 | 7 | 24.8 | 52.9 | 20.5 | 23.2 | 32.2 | 26.5 | 3.1 | 9.3 |
| Zn | 59 | 54 | 56.5 | 105 | 58 | 63 | 75 | 28 | 29 | 42 |
| Ni | 8.8 | 440.8 | 224.8 | 31.8 | 24.7 | 548.2 | 201.6 | 61.7 | 268.8 | 257.6 |
| Au (ppb) | 6.1 | 1.9 | 4 | 4.8 | 1.6 | 2.4 | 2.9 | 4.9 | 1.3 | 2.9 |
| Ag | <0.1 | <0.1 | <0.1 | <0.1 | <0.1 | <0.1 | <0.1 | <0.1 | <0.1 | <0.1 |
| Mo | 1.2 | 0.2 | 0.7 | 0.3 | 0.6 | <0.1 | <0.3 | 0.3 | 0.1 | 2.1 |
| Cu | 11.9 | 17.2 | 14.6 | 29.7 | 11.1 | 43.4 | 28.1 | 13.4 | 7.7 | 10.3 |
| As | 5.6 | 0.5 | 3.1 | 4.7 | 12.3 | 2.6 | 6.5 | 2.5 | 3.8 | 44.7 |
| Cd | 0.1 | <0.1 | <0.1 | 0.5 | <0.1 | 0.1 | <0.2 | 0.2 | 0.2 | <0.1 |
| Sb | 0.3 | 0.1 | 0.2 | 0.1 | 0.3 | <0.1 | <0.2 | 0.3 | <0.1 | 0.4 |
| Bi | 0.4 | 0.2 | 0.3 | 0.6 | 0.3 | 0.6 | 0.5 | 0.6 | <0.1 | 0.2 |
| Hg | 0.03 | 0.03 | 0.03 | 0.16 | <0.01 | 0.12 | <0.10 | 0.13 | 0.08 | 0.13 |
| $\sum$REE | 123.2 | 124.5 | 123.9 | 300.5 | 154.6 | 104.7 | 186.6 | 202.4 | 214.1 | 116.4 |
| $\sum$LREE | 97.41 | 93.11 | 95.26 | 233.6 | 119.21 | 92.75 | 148.51 | 144.97 | 173.3 | 91.82 |
| $\sum$MREE | 10.45 | 11.98 | 11.22 | 25.26 | 15.68 | 11.84 | 17.59 | 19.49 | 15.52 | 9.42 |
| $\sum$HREE | 2.71 | 3.95 | 3.33 | 7.13 | 3.85 | 3.96 | 4.98 | 6.11 | 4.67 | 2.75 |
| Eu/Eu* | 1.99 | 1.92 | 1.96 | 2.08 | 2.34 | 2.24 | 2.22 | 2.02 | 1.80 | 2.08 |
| Ce/Ce* | 0.77 | 0.75 | 0.76 | 1.89 | 0.95 | 0.74 | 1.19 | 1.28 | 1.41 | 0.74 |
| V/(V+Ni) | 0.8 | 0.1 | 0.45 | 0.8 | 0.4 | 0.1 | 0.43 | 0.4 | 0.2 | 0.2 |
| V/Cr | 1.7 | 0.04 | 0.8 | 1.1 | 8.1 | 0.1 | 3.1 | 0.3 | 0.03 | 0.08 |
| Ni/Co | 1.3 | 11.5 | 6.4 | 2.6 | 1.5 | 9.0 | 4.4 | 7.8 | 9.6 | 9.4 |
| Cu/Zn | 0.2 | 0.3 | 0.25 | 0.3 | 0.2 | 0.7 | 0.4 | 0.4 | 0.2 | 0.2 |

Orhaneli-Gümüşpınar area

| Major oxides (wt.%) | Sandstone | | Marl | | | Tuff/tuffite | | | |
|---|---|---|---|---|---|---|---|---|---|
| | C-14 | Ave | C-12 | C-22 | Ave | A6-25 | C-17 | C-20 | Ave |
| $SiO_2$ | 71.58 | 67.16 | 28.88 | 14.33 | 21.60 | 67.53 | 67.28 | 69.06 | 67.95 |
| $Al_2O_3$ | 10.36 | 11.85 | 8.69 | 4.40 | 6.54 | 13.24 | 13.91 | 12.90 | 13.35 |
| $Fe_2O_3$ | 2.14 | 3.72 | 3.45 | 2.36 | 2.90 | 2.15 | 1.13 | 1.39 | 1.55 |
| MgO | 2.18 | 2.42 | 2.82 | 3.21 | 3.01 | 1.11 | 1.42 | 1.66 | 1.40 |
| CaO | 2.68 | 3.90 | 25.71 | 33.60 | 29.65 | 1.24 | 1.47 | 2.30 | 1.67 |
| $Na_2O$ | 1.26 | 1.88 | 0.19 | 0.28 | 0.23 | 1.62 | 1.54 | 1.78 | 1.65 |
| $K_2O$ | 2.05 | 1.69 | 0.95 | 0.48 | 0.71 | 4.5 | 3.95 | 2.56 | 3.67 |
| $TiO_2$ | 0.15 | 0.28 | 0.37 | 0.19 | 0.28 | 0.10 | 0.12 | 0.09 | 0.10 |
| $P_2O_5$ | 0.05 | 0.08 | 0.05 | 0.15 | 0.1 | 0.02 | 0.02 | 0.02 | 0.02 |
| MnO | 0.04 | 0.05 | 0.02 | 0.20 | 0.11 | 0.06 | 0.06 | 0.02 | 0.05 |
| $Cr_2O_3$ | 0.038 | 0.19 | 0.031 | 0.017 | 0.024 | 0.058 | 0.008 | 0.013 | 0.03 |
| TOT/S | 0.09 | 0.27 | 0.04 | 0.38 | 0.21 | <0.02 | <0.02 | <0.02 | <0.02 |
| TOT/C | 0.53 | 0.56 | 6.26 | 9.73 | 7.99 | 0.03 | 0.02 | 0.10 | 0.05 |
| LOI | 7.0 | 6.47 | 28.6 | 35.2 | 31.9 | 8.2 | 9.0 | 8.1 | 8.4 |
| Total | 99.81 | 99.84 | 99.80 | 94.43 | 97.11 | 99.90 | 99.90 | 99.92 | 99.90 |
| CIW | 60.00 | 54.44 | 15.65 | 6.64 | 11.14 | 72.9 | 72.9 | 64.45 | 70.08 |
| Ba | 1977 | 977.33 | 377 | 310 | 343.5 | 157 | 308 | 334 | 266.3 |
| Cr | 260.0 | 1299.9 | 212.0 | 116.3 | 164.1 | 396.8 | 54.7 | 88.9 | 205.2 |

**Table 2** (continued)

| | | | | | | | | | |
|---|---|---|---|---|---|---|---|---|---|
| Co | 19.9 | 25.10 | 19.4 | 10 | 14.7 | 7.3 | 2.1 | 1.5 | 3.6 |
| Cs | 37.1 | 23.43 | 75.3 | 31.9 | 53.6 | 22.7 | 26.4 | 11.9 | 20.3 |
| Ga | 7.5 | 10.53 | 9.5 | 4.9 | 7.2 | 16.2 | 16.3 | 13.2 | 15.2 |
| Hf | 1.7 | 2.70 | 1.8 | 1.0 | 1.4 | 3.1 | 3.1 | 2.5 | 2.9 |
| Nb | 3.5 | 6.73 | 9.3 | 4.9 | 7.1 | 32.3 | 28.1 | 26.2 | 28.8 |
| Rb | 76 | 59.73 | 70.9 | 31.9 | 51.4 | 258.6 | 249.6 | 104.9 | 204.3 |
| Sn | <1 | <1 | <1 | <1 | <1 | 8 | 5 | 4 | 5.6 |
| Sr | 1042.2 | 572.1 | 756.1 | 667.4 | 711.7 | 50.1 | 74.3 | 124.7 | 83.0 |
| Ta | 0.3 | 0.6 | 0.3 | 0.3 | 0.3 | 4.4 | 3.2 | 2.1 | 3.2 |
| Th | 2.9 | 7.1 | 9.3 | 4.0 | 6.6 | 26.3 | 29.1 | 23 | 26.1 |
| U | 2.3 | 1.7 | 3 | 2.4 | 2.7 | 14 | 9.2 | 4.8 | 9.3 |
| V | 31 | 68 | 49 | 29 | 39 | 10 | 12 | 14 | 12 |
| W | 0.9 | 1.3 | 2.1 | 2.3 | 2.2 | 3.7 | 3.1 | 1.2 | 2.6 |
| Zr | 65.6 | 102.3 | 67.2 | 42.6 | 54.9 | 67.5 | 78.5 | 69.2 | 71.7 |
| Y | 8.7 | 14.0 | 9.8 | 7.2 | 8.5 | 36.8 | 26.5 | 13.5 | 25.6 |
| La | 8.5 | 26.0 | 19.4 | 10.9 | 15.1 | 19.6 | 21.6 | 18.2 | 19.8 |
| Ce | 17.8 | 49.9 | 35.9 | 19.2 | 27.5 | 35.9 | 44.2 | 32.2 | 37.4 |
| Pr | 2.02 | 5.35 | 4.04 | 2.19 | 3.1 | 4.27 | 4.80 | 3.79 | 4.3 |
| Nd | 8 | 19.3 | 14.3 | 7.5 | 10.9 | 15.2 | 16 | 13.9 | 15.0 |
| Sm | 1.55 | 3.40 | 2.71 | 1.49 | 2.1 | 4.10 | 3.91 | 3.08 | 3.7 |
| Eu | 0.39 | 0.75 | 0.63 | 0.40 | 0.5 | 0.26 | 0.35 | 0.39 | 0.3 |
| Gd | 1.53 | 2.71 | 2.17 | 1.48 | 1.8 | 4.69 | 3.80 | 2.60 | 3.7 |
| Tb | 0.20 | 0.40 | 0.31 | 0.22 | 0.2 | 0.90 | 0.69 | 0.42 | 0.67 |
| Dy | 1.30 | 2.35 | 1.73 | 1.34 | 1.5 | 6.12 | 4.35 | 2.54 | 4.3 |
| Ho | 0.27 | 0.46 | 0.32 | 0.29 | 0.3 | 1.28 | 0.88 | 0.43 | 0.8 |
| Er | 0.86 | 1.40 | 1.01 | 0.85 | 0.9 | 3.86 | 2.85 | 1.22 | 2.6 |
| Tm | 0.12 | 0.20 | 0.15 | 0.10 | 0.12 | 0.59 | 0.40 | 0.18 | 0.3 |
| Yb | 0.93 | 1.34 | 0.89 | 0.79 | 0.8 | 3.95 | 2.77 | 1.39 | 2.7 |
| Lu | 0.16 | 0.23 | 0.14 | 0.13 | 0.135 | 0.59 | 0.43 | 0.21 | 0.4 |
| Pb | 8.4 | 6.9 | 13.3 | 7.1 | 10.2 | 8.9 | 11.1 | 9.9 | 10.0 |
| Zn | 21 | 31 | 40 | 21 | 30.5 | 21 | 13 | 13 | 15.6 |
| Ni | 209.9 | 245.4 | 187.4 | 83.3 | 135.3 | 63.6 | 15.5 | 23.7 | 34.2 |
| Au (ppb) | 2 | 2.1 | 4 | 0.8 | 2.4 | 2.8 | 2 | 5.6 | 3.4 |
| Ag | <0.1 | <0.1 | <0.1 | <0.1 | <0.1 | <0.1 | <0.1 | <0.1 | <0.1 |
| Mo | 0.6 | 0.9 | 0.4 | 0.5 | 0.45 | <0.1 | <0.1 | <0.1 | <0.1 |
| Cu | 11 | 9.7 | 23.9 | 11.7 | 17.8 | 2.9 | 2.2 | 1.6 | 2.2 |
| As | 35.4 | 28.0 | 10.9 | 26.2 | 18.5 | <0.5 | <0.5 | 0.7 | 0.5 |
| Cd | 0.2 | <0.2 | 0.2 | <0.1 | <0.15 | <0.1 | <0.1 | <0.1 | <0.1 |
| Sb | 0.2 | <0.2 | 0.2 | 0.3 | 0.25 | <0.1 | 0.2 | 0.1 | <0.1 |
| Bi | <0.1 | <0.1 | 0.2 | 0.1 | 0.15 | 0.5 | 0.5 | 0.3 | 0.4 |
| Hg | 0.07 | 0.09 | 0.07 | 0.03 | 0.05 | 0.17 | 0.03 | 0.02 | 0.07 |
| $\sum$REE | 52.33 | 127.60 | 93.5 | 54.08 | 73.7 | 138.11 | 133.53 | 94.05 | 121.89 |
| $\sum$LREE | 36.32 | 100.48 | 73.64 | 39.79 | 56.71 | 74.97 | 86.6 | 68.09 | 76.55 |
| $\sum$MREE | 5.24 | 10.06 | 7.87 | 5.22 | 6.54 | 17.35 | 13.98 | 9.46 | 13.59 |
| $\sum$HREE | 2.07 | 3.16 | 2.19 | 1.87 | 2.03 | 8.99 | 6.45 | 3.00 | 6.14 |
| Eu/Eu* | 2.03 | 1.97 | 1.92 | 2.15 | 2.03 | 0.94 | 1.04 | 1.18 | 1.05 |
| Ce/Ce* | 0.28 | 0.81 | 0.61 | 0.34 | 0.47 | 0.63 | 0.70 | 0.57 | 0.63 |

**Table 2** (continued)

| | | | | | | | | | | |
|---|---|---|---|---|---|---|---|---|---|---|
| V/(V + Ni) | 0.1 | 0.16 | 0.2 | 0.2 | 0.2 | 0.1 | 0.4 | 0.3 | 0.3 | |
| V/Cr | 0.1 | 0.07 | 0.2 | 0.2 | 0.2 | 0.02 | 0.2 | 0.1 | 0.1 | |
| Ni/Co | 10.5 | 9.8 | 9.6 | 8.3 | 8.9 | 8.7 | 7.3 | 15.8 | 10.6 | |
| Cu/Zn | 0.5 | 0.3 | 0.6 | 0.5 | 0.5 | 0.1 | 0.2 | 0.1 | 0.1 | |

Keles-Harmanalan area

| Major oxides (wt.%) | Organic-rich shale | Argillaceous sediment | | | | | | Mudstone | Marl | Tuff |
|---|---|---|---|---|---|---|---|---|---|---|
| | H16-9 | H16-14 | H16-5 | H16-13 | H16-2-5 | H16-18 | Ave | H16-3 | H16-2-4 | H16-7 |
| $SiO_2$ | 32.91 | 22.88 | 54.03 | 40.97 | 62.99 | 64.21 | 49.01 | 74.41 | 37.61 | 51.70 |
| $Al_2O_3$ | 16.02 | 16.42 | 19.64 | 20.00 | 13.27 | 13.80 | 16.62 | 13.87 | 8.34 | 22.37 |
| $Fe_2O_3$ | 2.46 | 18.86 | 4.62 | 2.82 | 2.39 | 4.82 | 6.70 | 3.15 | 1.68 | 4.97 |
| MgO | 1.68 | 0.81 | 1.57 | 1.92 | 3.18 | 2.75 | 2.04 | 1.01 | 2.45 | 1.20 |
| CaO | 1.08 | 3.19 | 2.80 | 0.77 | 2.0 | 1.13 | 1.97 | 0.16 | 23.17 | 3.15 |
| $Na_2O$ | 0.43 | 0.32 | 0.41 | 0.29 | 1.41 | 0.6 | 0.60 | 0.62 | 0.42 | 0.21 |
| $K_2O$ | 2.13 | 2.90 | 9.50 | 3.33 | 2.96 | 2.74 | 4.28 | 0.51 | 1.49 | 8.53 |
| $TiO_2$ | 0.64 | 0.30 | 0.65 | 0.77 | 0.19 | 0.58 | 0.50 | 0.81 | 0.17 | 0.63 |
| $P_2O_5$ | 0.02 | 5.18 | 0.58 | 0.04 | 0.03 | 0.14 | 1.19 | 0.02 | 0.07 | 0.25 |
| MnO | 0.02 | 0.04 | 0.07 | 0.02 | 0.06 | 0.03 | 0.04 | 0.04 | 0.03 | 0.07 |
| $Cr_2O_3$ | 0.020 | <0.002 | 0.003 | 0.018 | 0.175 | 0.014 | 0.042 | 0.016 | 0.027 | 0.006 |
| TOT/S | 1.03 | 13.78 | 0.28 | 0.59 | 0.02 | 0.40 | 3.01 | 0.18 | 0.73 | 0.85 |
| TOT/C | 23.42 | 5.68 | 0.12 | 13.97 | 0.05 | 0.28 | 4.02 | 0.08 | 5.47 | 0.07 |
| LOI | 42.4 | 27.7 | 5.3 | 28.8 | 11.11 | 8.9 | 16.36 | 5.3 | 24.4 | 6.1 |
| Total | 99.82 | 98.92 | 99.51 | 99.81 | 99.84 | 99.82 | 99.58 | 99.89 | 99.84 | 99.52 |
| CIW | 85 | 72.29 | 77.30 | 91.48 | 69.14 | 82.06 | 78.45 | 91.55 | 16 | 78.77 |
| Ba | 414 | 3078 | 3406 | 559 | 228 | 356 | 1525.4 | 82 | 231 | 2724 |
| Cr | 136.8 | 13.6 | 20.5 | 123.1 | 1197.3 | 95.8 | 287.3 | 109.4 | 184.7 | 41.0 |
| Co | 8.2 | 7.3 | 21.6 | 7.7 | 14.1 | 9.4 | 12.02 | 7.8 | 4.8 | 12.2 |
| Cs | 60.9 | 10.7 | 25.1 | 92.7 | 90 | 54.7 | 54.6 | 6.5 | 15.1 | 19 |
| Ga | 19.9 | 10.8 | 24 | 23.2 | 16.7 | 15.5 | 18.0 | 13 | 9.6 | 25.7 |
| Hf | 3.9 | 3.6 | 9.8 | 3.9 | 3.6 | 5.6 | 5.3 | 7.1 | 2.3 | 10.5 |
| Nb | 14.9 | 3.9 | 28.3 | 16.4 | 34.8 | 11.9 | 19.0 | 14 | 13.9 | 37 |
| Rb | 141.8 | 77.5 | 247.1 | 210 | 250 | 171.9 | 191.3 | 27.1 | 59.5 | 199 |
| Sn | 3 | <1 | 2.0 | 5 | 6 | 2 | 3.2 | 2 | 2 | 2 |
| Sr | 420.6 | 8223.5 | 1604.2 | 278.9 | 127.4 | 202.7 | 2087.3 | 72.4 | 574.1 | 1582.6 |
| Ta | 1.1 | 0.5 | 1.2 | 1.1 | 3.4 | 0.8 | 1.4 | 1.2 | 1.2 | 1.3 |
| Th | 13.8 | 40.2 | 79.4 | 22.5 | 23.7 | 16.4 | 36.4 | 16 | 15.8 | 74.8 |
| U | 6.4 | 7.5 | 19.8 | 4.9 | 7.1 | 5.5 | 8.9 | 2.6 | 5.3 | 17.2 |
| V | 129 | 33 | 109 | 121 | 41 | 112 | 83.2 | 76 | 31 | 139 |
| W | 2.6 | 1.4 | 0.8 | 2.9 | 2.6 | 2 | 1.9 | 2 | 1 | 1.8 |
| Zr | 141.3 | 146.1 | 472.8 | 143.4 | 92.1 | 194.4 | 209.8 | 257.3 | 83.7 | 504.8 |
| Y | 29.1 | 41.5 | 48.7 | 32.7 | 31.7 | 24.1 | 35.7 | 25.4 | 20.4 | 40.3 |
| La | 28.1 | 57.2 | 225.4 | 43.7 | 15 | 41.7 | 76.6 | 32.7 | 22.7 | 220.8 |
| Ce | 48 | 100.9 | 401.3 | 81.4 | 32.1 | 78.9 | 138.9 | 65.2 | 40.4 | 429.7 |
| Pr | 6.25 | 11.11 | 46.37 | 9.85 | 3.80 | 9.68 | 16.1 | 7.7 | 4.41 | 46.4 |
| Nd | 25.5 | 44.4 | 184.6 | 38.6 | 15.2 | 38.3 | 64.2 | 30.7 | 16.1 | 172.5 |
| Sm | 5.34 | 8.47 | 28.77 | 7.99 | 4.40 | 6.15 | 11.1 | 6.68 | 3.42 | 25.65 |
| Eu | 1.05 | 1.94 | 6.61 | 1.5 | 0.36 | 1.20 | 2.3 | 1.48 | 0.45 | 5.92 |
| Gd | 5.41 | 8.08 | 18.96 | 6.85 | 4.46 | 5.42 | 8.75 | 5.72 | 3.09 | 15.66 |

**Table 2** (continued)

| Tb | 0.83 | 1.02 | 2.28 | 1.02 | 0.80 | 0.73 | 1.17 | 0.81 | 0.46 | 1.78 |
|---|---|---|---|---|---|---|---|---|---|---|
| Dy | 5.02 | 6.32 | 10.73 | 5.90 | 5.17 | 4.42 | 6.5 | 4.62 | 2.82 | 8.07 |
| Ho | 1.05 | 1.26 | 1.62 | 1.05 | 1.1 | 0.84 | 1.17 | 0.95 | 0.58 | 1.28 |
| Er | 2.95 | 2.94 | 3.86 | 2.85 | 3.36 | 2.31 | 3.0 | 2.57 | 2.02 | 2.96 |
| Tm | 0.40 | 0.32 | 0.49 | 0.37 | 0.45 | 0.31 | 0.38 | 0.37 | 0.28 | 0.37 |
| Yb | 2.83 | 1.84 | 3.14 | 2.43 | 3.24 | 2.21 | 2.5 | 2.49 | 1.85 | 2.49 |
| Lu | 0.45 | 0.23 | 0.42 | 0.36 | 0.5 | 0.33 | 0.37 | 0.38 | 0.29 | 0.32 |
| Pb | 33.4 | 44.6 | 98.9 | 44.9 | 19.9 | 21.6 | 46.0 | 23 | 21.4 | 107.9 |
| Zn | 46 | 47 | 92 | 40 | 24 | 46 | 49.8 | 36 | 20 | 72 |
| Ni | 30.4 | 27.3 | 19.5 | 20.3 | 117.9 | 20.8 | 21.1 | 27.4 | 26.1 | 18.8 |
| Au (ppb) | 6.6 | 5.9 | 9.8 | 4.0 | 0.8 | 1.4 | 4.3 | 5.4 | 3.2 | 6.2 |
| Ag | 0.1 | <0.1 | <0.1 | <0.1 | <0.1 | <0.1 | <0.1 | <0.1 | <0.1 | 0.1 |
| Mo | 1.6 | 1.3 | <0.1 | 0.5 | 0.3 | 0.2 | 0.4 | 0.1 | 0.5 | 0.8 |
| Cu | 33.4 | 11 | 46.3 | 36.2 | 9 | 14.8 | 23.4 | 19.2 | 4.8 | 33.3 |
| As | 6.8 | 65.2 | 4.9 | 2.3 | 1.1 | 21.8 | 19.0 | 1.0 | 32.8 | 8.6 |
| Cd | 0.3 | 0.2 | <0.1 | 1.0 | <0.1 | 0.2 | 0.32 | <0.1 | 0.1 | <0.1 |
| Sb | 0.4 | 6.5 | 0.31 | 0.5 | 0.3 | 0.1 | 1.54 | 0.1 | 0.1 | 0.6 |
| Bi | 0.6 | 0.6 | 1.3 | 0.8 | 0.5 | 0.3 | 0.7 | 0.3 | 0.4 | 0.8 |
| Hg | 0.16 | 0.66 | 0.01 | 0.29 | 0.04 | 0.07 | 0.21 | 0.03 | 0.03 | 0.08 |
| $\Sigma$REE | 162.28 | 287.53 | 983.25 | 236.57 | 121.64 | 216.6 | 369.1 | 187.77 | 119.27 | 974.2 |
| $\Sigma$LREE | 107.85 | 213.61 | 857.67 | 173.55 | 66.1 | 192.68 | 300.72 | 136.3 | 83.61 | 869.4 |
| $\Sigma$MREE | 18.7 | 27.09 | 68.97 | 24.31 | 16.29 | 18.76 | 31.0 | 20.26 | 10.82 | 58.36 |
| $\Sigma$HREE | 6.63 | 5.33 | 7.91 | 6.01 | 7.55 | 5.16 | 6.39 | 5.81 | 4.44 | 6.14 |
| Eu/Eu* | 1.92 | 2.27 | 2.93 | 1.96 | 1.04 | 1.87 | 2.0 | 2.11 | 1.24 | 2.68 |
| Ce/Ce* | 0.91 | 1.74 | 7.02 | 1.43 | 0.52 | 1.38 | 2.41 | 1.09 | 0.69 | 6.95 |
| V/(V+Ni) | 1.2 | 0.5 | 0.8 | 0.8 | 0.2 | 0.8 | 0.6 | 0.7 | 0.5 | 0.9 |
| V/Cr | 0.9 | 2.4 | 5.3 | 0.9 | 0.03 | 1.1 | 1.9 | 0.7 | 0.1 | 3.3 |
| Ni/Co | 3.7 | 3.7 | 0.9 | 2.6 | 8.3 | 2.2 | 3.5 | 3.5 | 5.4 | 1.5 |
| Cu/Zn | 0.7 | 0.2 | 0.5 | 0.9 | 0.3 | 0.3 | 0.4 | 0.5 | 0.2 | 0.4 |

$\Sigma$REE = the sum of (La–Lu) + Y; $\Sigma$LREE = the sum of La–Nd; $\Sigma$MREE = the sum of (Sm–Ho); $\Sigma$HREE = the sum of (Er–Lu);

Eu/Eu* = Eu$_N$/ [(Sm$_N$x0.67) + (Tb$_N$x0.33)] (Bau & Dulski, 1996) and Ce/Ce* = 0.5La$_N$ + 0.5Pr$_N$. (Dai et al., 2016) LOI: loss on ignition at 1050°C

correlation and Al$_2$O$_3$ vs. CaO ($r^2$ = 0.67) shows a negative correlation in the tuff/tuffite, marl, organic-rich shale, sandstone mudstone, and argillaceous sediment samples (Fig. 11b).

The large iron oxide content (up to 8.69 and 18.86 wt.%) and the total S content (TOT/S) (up to 0.96 and 13.78 wt.%) are determined in argillaceous sediments of Orhaneli-Gümüşpınar and Keles-Harmanalan areas, respectively. The total carbon (TOT/C) values show max. 9.73 and 5.47 wt.% in marls, and max. 12.08 and 23.42 wt.% of organic-rich shale in the Orhaneli-Gümüşpınar and Keles-Harmanalan areas, respectively.

The chemical index of weathering (CIW) values of the parent rocks increase toward the argillaceous sediments (up to 92.59 except for organic-rich shale and 91.48 except mudstone) of the Orhaneli-Gümüşpınar and Keles-Harmanalan areas, respectively (Table 2).

**Trace elements** Ba (up to 662 and 3406 ppm), Sr (up to 304.7 and 8223.5 ppm), Zr (up to 171.8 and 472.8 ppm), Co (up to 60.5 and 21.6 ppm), Cr (up to 513.2 and 1197.4 ppm), Ni (up to 548.2 and 117.9 ppm), Cu (up to 43.4 and 46.3 ppm), and Zn (up to 105 and 92 ppm) values in argillaceous sediments of the Orhaneli-Gümüşpınar and

Keles-Harmanalan area, respectively, exhibit large values compared to those of the volcanogenic and terrigenous sediments (Table 2).

The ratios of Ni/Co (0.9–15.8), V/(V + Ni) (0.1–0.8), V/Cr (0.03–8.1), and Cu/Zn (0.1–0.9) were determined (Table 2). In terms of element correlations, $K_2O$ correlated positively with Rb ($r^2 = 0.74$) (Fig. 11c). The plot of $Al_2O_3$ vs. Th ($r^2 = 0.50$), $Al_2O_3$ vs. Zr ($r^2 = 0.55$), $Al_2O_3$ vs. Y ($r^2 = 0.48$), and Nb vs. Y ($r^2 = 0.60$) also showed positive correlations (Fig. 11d–g).

**Rare earth elements (REE)** Whole-rock REE abundances for the marl, parent rocks (tuff/tuffite, organic-rich shale, sandstone, mudstone), and argillaceous sediments were normalized to Upper Continental Crust (UCC) values (Fig. 12; Taylor & McLennan, 1985). The average range of ΣREE values of the parent rocks and argillaceous sediments are 73.7–974.2 and 186.6–369.1 ppm, respectively (Fig. 13). The average ΣLREE and ΣHREE values of the parent rocks and argillaceous sediments are 56.71–869.4 and 148.51–300.72 ppm, 4.44–6.14 and 4.98–6.39 ppm, respectively (Table 2). The average light rare earth elements (LREE) exhibit slight enrichment relative to heavy rare earth elements (HREE) concentrations of the parent rocks and argillaceous sediments. The

Eu anomaly (0.94–2.34 and 1.04–2.93) showed positive values in the Orhaneli-Gümüşpınar and Keles-Harmanalan areas, respectively (Table 2). The Ce value showed a negative anomaly (0.28–0.95 except for samples A6-16, A6-22, and A6-1) in Orhaneli-Gümüşpınar and positive anomalies (1.09–6.95 except samples H16-2–4, H16-9, and H16-2–5) in the Keles-Harmanalan area (Table 2). Rb and Nb show negative anomalies.

**Smectite chemistry** The structural formula of montmorillonitic smectite was calculated from the chemical analysis of the clay fractions (Table 3) as follows:

$$(Ca_{0.42}Na_{0.25}K_{0.08})(Al_{2.76}Fe_{0.47}Mg_{0.59}Ti_{0.07}Mn_{0.002})(Si_{7.65}Al_{0.35})O_{20}(OH)_4$$
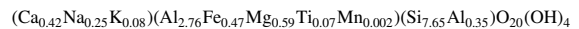
This formula was constructed by filling the tetrahedral sites with all of the Si and Al, and the octahedral cations included the remaining Al and Fe(III), Mg, Ti, and $Mn^{2+}$. The $SiO_2/Al_2O_3$ ratio is 2.90 compatible with montmorillonite (Christidis & Dunham, 1997).

The tetrahedral/octahedral charge ratio ($x_t/x_o$) of smectites was 0.42, consistent with montmorillonite (Güven, 1988). The $Na^+/(Na^+ + Ca^{2+})$ ratios of the smectite, 0.75, was determined as Na-Ca-smectites (Table 3; Takagi et al., 2005).
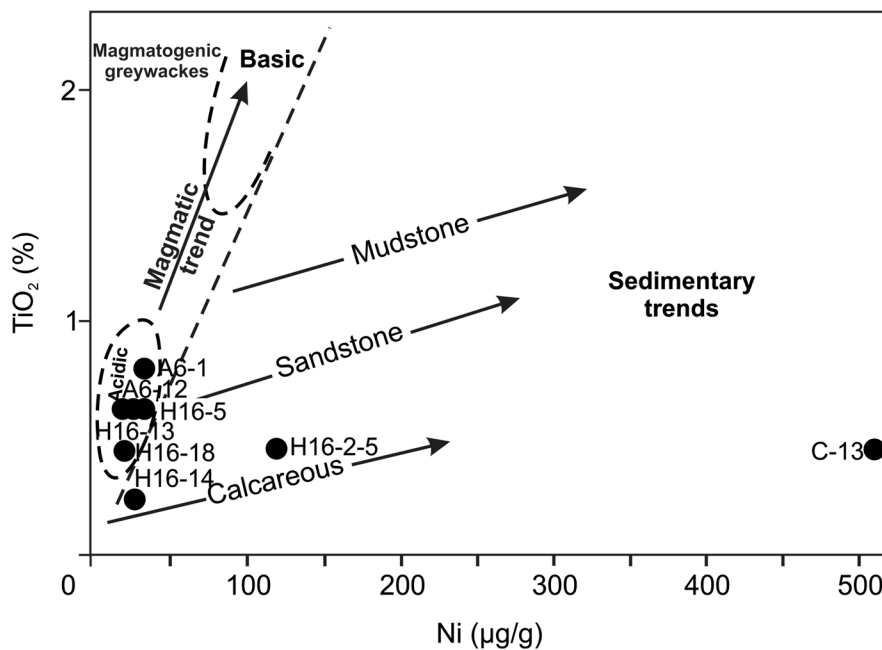


**Fig. 9** Provenance diagram of Ni vs. $TiO_2$ in the argillaceous sediment samples studied (after Floyd et al., 1989)
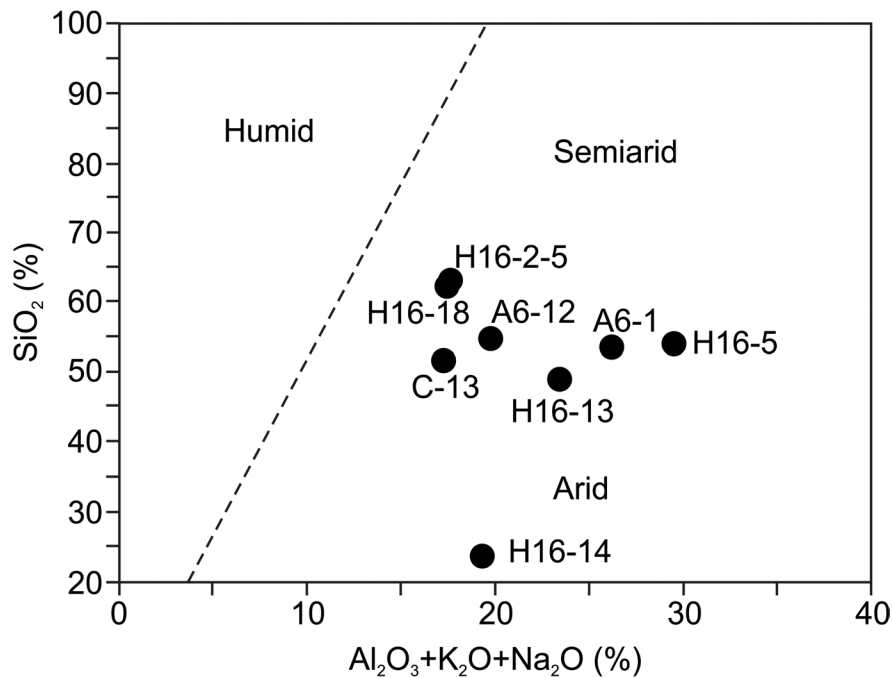
**Fig. 10** Paleoclimate discrimination diagram of $SiO_2$ vs. $(Al_2O_3 + K_2O + Na_2O)$ in the argillaceous sediment samples studied (after Suttner & Dutta, 1986)

**Stable isotope geochemistry** The O- and H-isotopic compositions of the puri0fied smectite and illite samples from the study area range from 1.39 to 9.13‰ and –64.24 to –87.61‰, respectively (Table 4 and Fig. 14). The samples plot to the left side of the supergene–hypogene line and close to the magmatic water box. The correlation of $\delta^{18}O$ with $Fe_2O_3$ in smectite shows a negative trend (Table 4).

The wide range of positive and negative $\delta^{34}S$ of pyrite and chalcopyrite samples from Bursa-Orhaneli-Keles range from –19.2 to 15 and from –16.4 to –1.5‰, respectively (Table 5). Pyrite-chalcopyrite pairs yield isotope equilibrium temperatures of 104.2–152.1°C using the equations of Ohmoto and Rye (1979).

$$T = (0.67 \pm 0.04)^{*}10^{3}/\delta^{34}S_{pyrite-}/\delta^{34}S_{chalcopyrite})^{1/2}$$

## Discussion

Depositional Environment of Clays

The argillaceous sediments in the Bursa-Orhaneli and Keles-Harmanalan coal mines were developed in a swampy and lacustrine environment in an E–W-trending graben system (west Anatolia) controlled by an extensional tectonic regime associated with volcanism and geothermal activities (Şengüler, 2004). The alteration of Triassic–Eocene metamorphic, ophiolitic, and igneous rocks (granitoid) of the basement by tectonic activity, alternation of warm and subtropical temperature, and rainfall regime favored the formation of clay-bearing detrital materials similar to those reported by Sáez et al. (2003).

In the first stage, the increase in the amount of terrigenous fluvial input toward the Keles-Harmanalan basin favored the deposition of detrital smectite in the organic-rich shale, mudstone, and sandstone (Figs. 3 and 15), and continued with an input of volcanic material upward in the sequence (Fig. 15). Consequently, in the second stage, the volcanic material was subjected to extensive alteration under diagenetic conditions (Fig. 15). Thus, smectite shows a detrital origin from terrigenous material and an authigenic origin in claystone which originated from the volcanic units.

Paleoclimate and paleoenvironment

The enrichment of *Bisaccat pollen* in the Upper Coal Seam is indicative of a dry, warm to subtropical
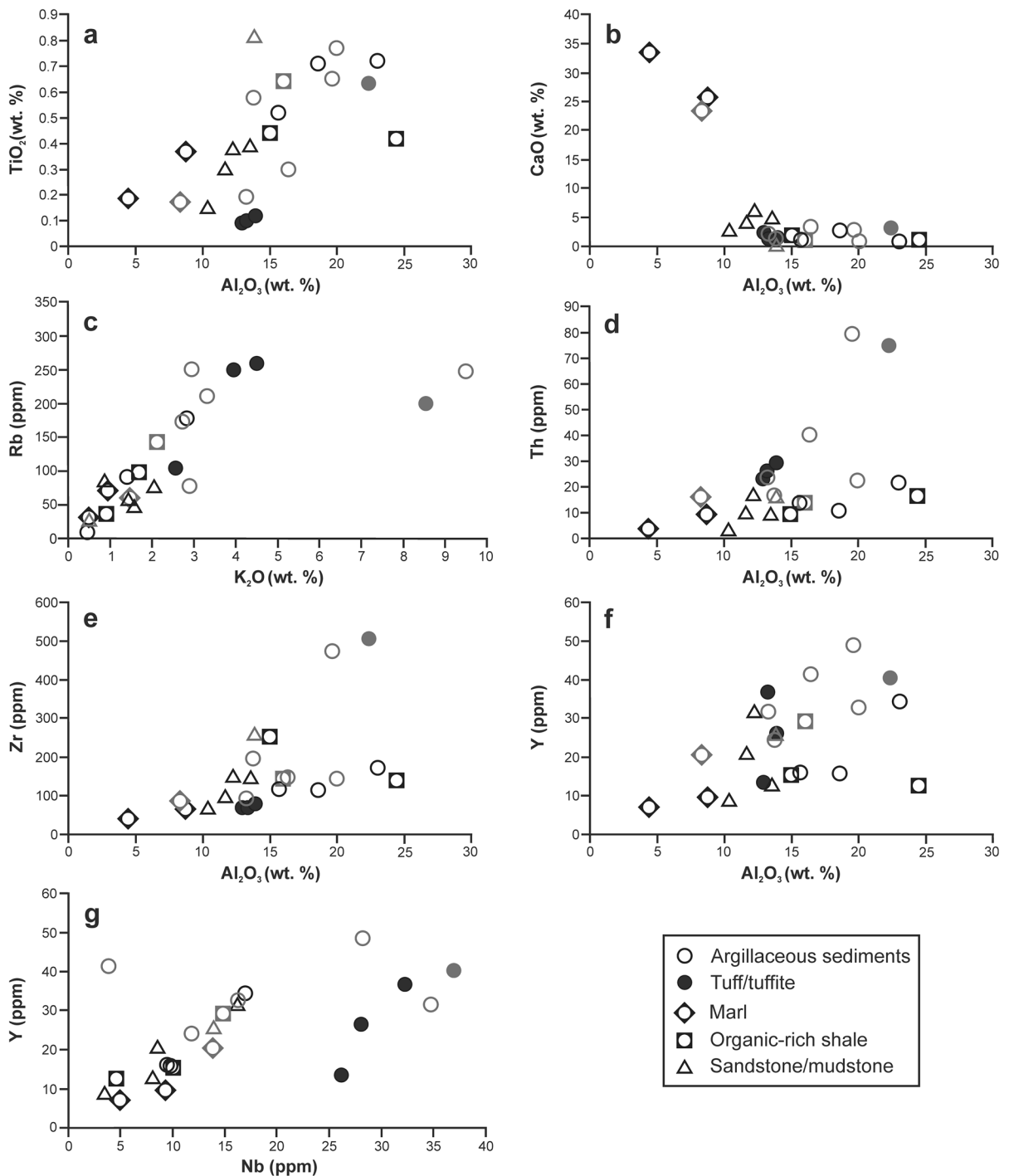
**Fig. 11** Elemental variation diagrams for major oxides (wt.%) and trace elements (ppm) of the Orhaneli-Gümüşpınar and Keles-Harmanalan argillaceous sediment, tuff/tuffite, marl, organic-rich shale, and sandstone/mudstone samples: **a** $Al_2O_3$ vs. $TiO_2$; **b** $Al_2O_3$ vs. CaO; **c** $K_2O$ vs. Rb; **d** $Al_2O_3$ vs. Th; **e** $Al_2O_3$ vs. Zr; **f** $Al_2O_3$ vs. Y; **g** Nb vs. Y. (The black and gray symbols represent samples from the Gümüşpınar and Keles areas, respectively)

🌱 Springer
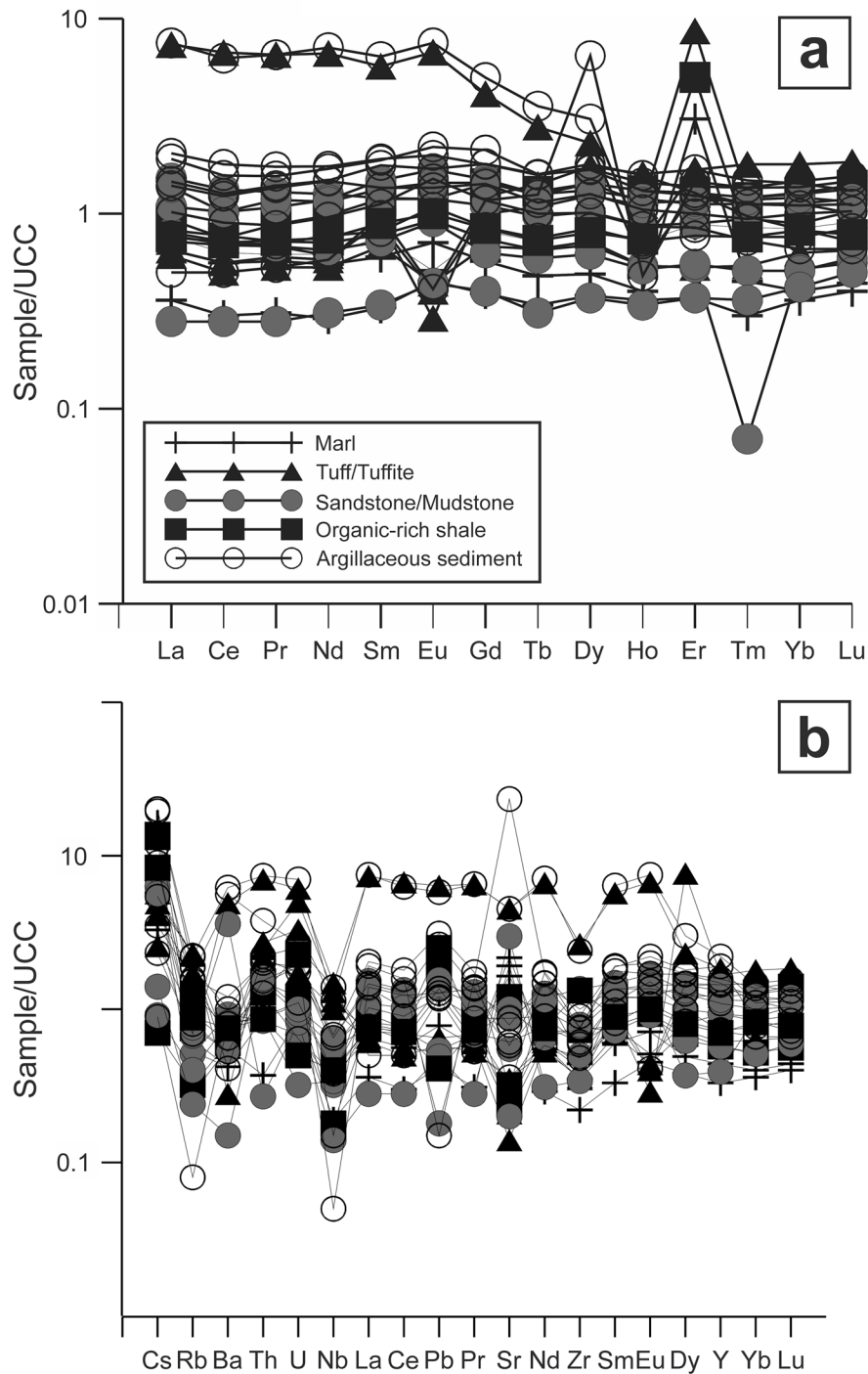
**Fig. 12** UCC-normalized **a** REE and **b** trace element patterns of tuff/tuffite, marl, organic-rich shale, sandstone/mudstone, and argillaceous sediment samples from the Orhaneli-Gümüşpınar and Keles-Harmanalan region (Taylor & McLennan, 1985)

climate in a continental area (Wheeler & Götz, 2017). The algal forms of *Botryococcus braunii* formed in fresh water and lakes in the study area (Sezgül Kayseri & Akgün, 2008).
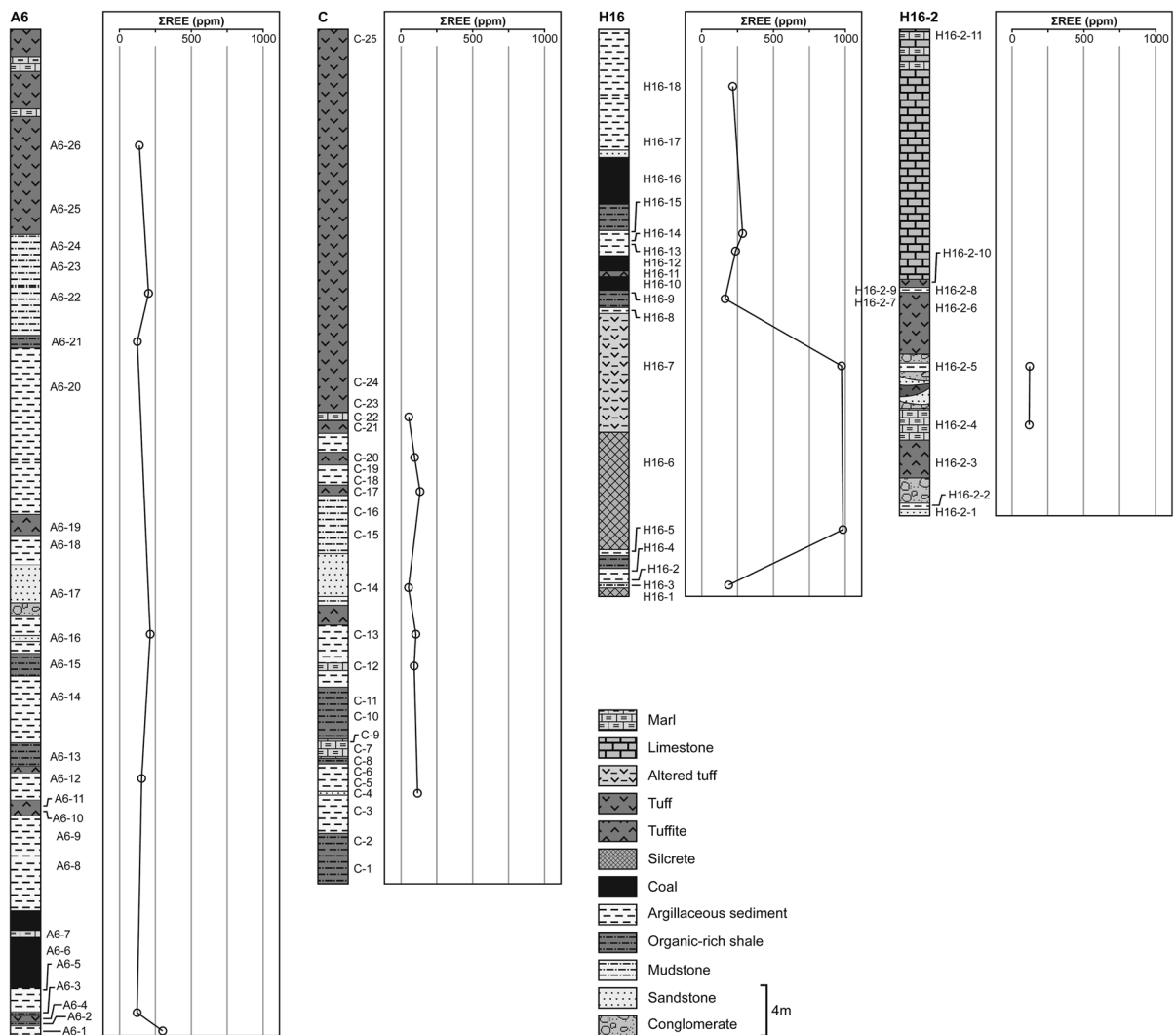
**Fig. 13** Variation in ΣREE values in the graphical log of argillaceous sediments and their parent rocks

The presence of sporomorphs such as *Intratripollenites instructus, Inaperturopollenites hiatus*, and *Subtriporopollenites simplex* in the organic-rich shale suggested that the sediments were deposited during the Late Eocene to Middle Miocene period (Benda et al., 1974; Nakoman, 1968; Roche & Schuler, 1980). The plot of $SiO_2$ vs. $(Al_2O_3 + K_2O + Na_2O)$ on the paleoclimate discrimination diagram suggests arid and semi-arid paleoclimate conditions in the study area, similar to those reported for the Huainan Coal basin, China (Chen et al., 2016).

**Mineralogical proof from argillaceous sediment and parent-rock samples**

The sharp-edged, irregularly-shaped, poorly-sorted quartz in thin sections from the study area suggest a pyroclastic origin, with monomineralic, well sorted, subrounded quartz having a terrigenous origin that was affected partially by the silica-rich hydrothermal fluid that favored the increase of quartz in sandstone, tuffite, and argillaceous sediments similar to the coal and tonsteins of Yunnan-China (Zhao et al., 2016). Furthermore, the metamorphic, ophiolitic,

**Table 3** Chemical composition (wt.%) and structural formula of a purified smectite sample

| Major oxides (wt.%) | A6-12 Na-Ca smectite |
|---|---|
| $SiO_2$ | 53.99 |
| $Al_2O_3$ | 18.57 |
| $\Sigma Fe_2O_3$ | 4.43 |
| MgO | 2.79 |
| CaO | 2.75 |
| $Na_2O$ | 0.92 |
| $K_2O$ | 0.46 |
| $TiO_2$ | 0.71 |
| $P_2O_5$ | 0.11 |
| MnO | 0.02 |
| LOI | 15.0 |
| Total | 99.85 |
| $SiO_2/Al_2O_3$ | 2.90 |
| Tetrahedral | |
| Si | 7.65 |
| Al | 0.35 |
| $\Sigma$ | 8.00 |
| Octahedral | |
| Al | 2.76 |
| Fe | 0.47 |
| Mg | 0.59 |
| Ti | 0.07 |
| Mn | 0.002 |
| $\Sigma$ | 3.89 |
| Interlayer | |
| Ca | 0.42 |
| Na | 0.25 |
| K | 0.08 |
| $\Sigma$ | 0.75 |
| $Na^+/(Na^+ + Ca^{2+})$ | 0.75 |
| Tetrahedral charge | 0.35 |
| Octahedral charge | 0.83 |
| Total charge | 1.18 |
| Interlayer charge | 1.20 |
| xt/xo | 0.42 |

and quartzite rock fragments were the main source of detrital input. In addition, fracture-filling pyrite and chalcopyrite suggest the contribution of hydrothermal fluids. The presence of pyrite and chalcopyrite in coal seams, organic-rich shale, and marl exhibit the influence of sulfate-rich groundwater and/or hydrothermal fluids in a reducing environment based on

S-isotope analysis similar to those reported by Jiang et al. (2016).

Examinations of the mineralogy and micromorphology showed that the relative increase in smectite and associated quartz, amphibole, and accessory chlorite, and the decrease in feldspar in argillaceous sediments, organic-rich shale, mudstone, and sandstone, compared to those in the volcanic units, and the significant degradation of quartz in detrital sediments suggest that smectite had a detrital origin in these units (Table 1 and Figs. 5 and 6a, b). In contrast, the close association of smectite with feldspar, the volcanic glass in a tuffaceous unit of the Bursa-Orhaneli and Keles-Harmanalan basins and the absence or rare presence of small amounts of detrital sediments such as quartz, amphibole, and chlorite suggest that smectite was formed authigenically (Table 1 and Figs. 5, 6c, and 7; Aldega et al., 2009; Leggo et al., 2001). The association of kaolinite with feldspar, biotite, and muscovite suggests that degradation of these precursor minerals resulted in the leaching of Na, Ca, and K through flushing by groundwater or hydrothermal fluid of organic-rich shale, mudstone, sandstone, and tuff/tuffite under an open acidic hydrologic system all of which favored the formation of kaolinite (Ece et al., 2013). The SEM analyses showed that illite edging smectite in the organic-rich shale, sandstone, and tuff/tuffite suggested that the degradation of smectite favored the formation of illite via dissolution and precipitation under alkaline conditions during early diagenesis (Çiflikli et al., 2013; Hower et al., 1976).

The presence of blocky, euhedral heulandite/clinoptilolite crystals in argillaceous sediments, sandstone, and tuff/tuffite suggest the contribution of volcanogenic materials and formation at pH < 11 conditions similar to those reported by Esenli et al. (2019).

The presence of siderite in sandstone, mudstone, organic-rich shale, and argillaceous sediments indicated the reaction of carbon dioxide with iron-bearing minerals (biotite, pyroxene) under a reducing environment (Reinink-Smith, 1990).

Geochemical Evidence from Major Oxides and Trace Elements of the Argillaceous Sediment and Host-rock Samples

Argillaceous sediment and host-rock (rhyolitic tuff/andesitic tuffite) samples have average $Al_2O_3/TiO_2$

Springer

**Table 4** Oxygen-hydrogen-isotopic compositions of smectite and illite from the study area

| Sample | Mineral | %H | δD V-SMOW (‰) | %O | δ18O V-SMOW (‰) | %Fe2O3 |
|---|---|---|---|---|---|---|
| A6-1 | Illite | 1.24 | −85.00 | 9.98 | 6.04 | 4.84 |
| A6-12 | Smectite | 0.92 | −68.90 | 5.80 | 5.00 | 4.43 |
| A6-21 | Smectite | 1.15 | −87.61 | 8.59 | 1.39 | 7.73 |
| A6-25 | Smectite | 1.19 | −80.08 | 9.10 | 7.84 | 2.15 |
| C-13 | Smectite | 1.39 | −68.88 | 11.31 | 5.09 | 8.69 |
| C-17 | Smectite | 1.17 | −68.93 | 8.92 | 8.68 | 1.13 |
| H16-5 | Smectite | 0.96 | −64.24 | 8.54 | 9.13 | 4.62 |
| H16-18 | Smectite | 1.07 | −67.37 | 9.21 | 7.01 | 4.82 |
| H16-2–5 | Smectite | 1.36 | −72.86 | 10.75 | 8.07 | 2.39 |
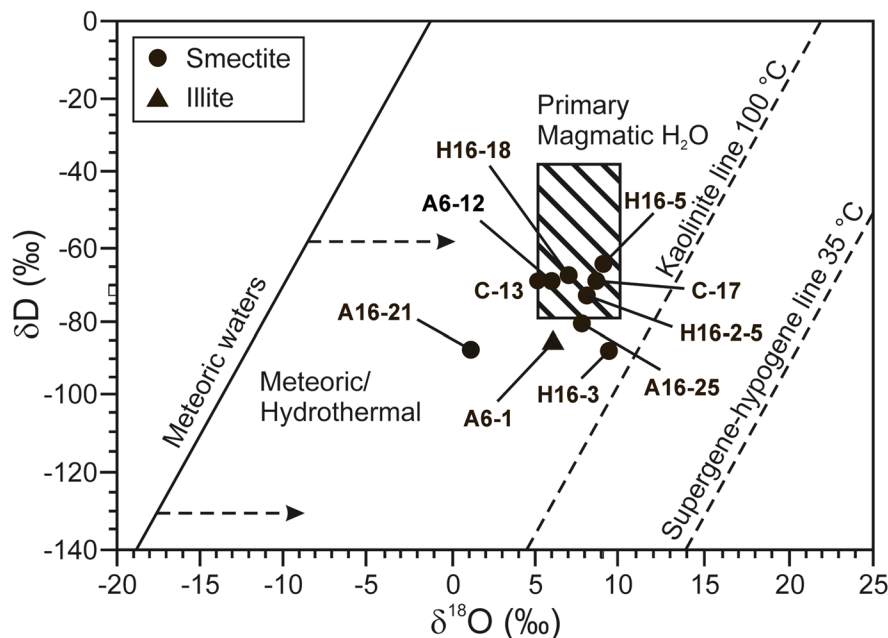


**Fig. 14** δD vs. δ18O plot showing isotopic compositions of smectite and illite from the Orhaneli-Gümüşpınar and Keles-Harmanalan region (Sheppard, 1986). The supergene/hypogene kaolinite equilibrium line with meteoric water at 35°C is from Sheppard et al. (1969). The kaolinite line in equilibrium with meteoric water at a temperature of 100°C is from Hayba et al. (1985). The meteoric water line is from Craig (1961)

**Table 5** δ34S composition of pyrite, and chalcopyrite samples from the study area

| Sample | Mineral | δ34S (‰) |
|---|---|---|
| A6-27 | Pyrite | −3.2 |
| H16-6 | Pyrite | 15.0 |
| H16-12A | Pyrite | −19.2 |
| A6-28 | Chalcopyrite | −1.5 |
| H16-12B | Chalcopyrite | −16.4 |

values 29.34–33.24 and 133.5–35.50, respectively, indicating that the volcanic parent rocks had an acidic character in Orhaneli-Gümüşpınar and intermediate to acidic in the Keles-Harmanalan basin with a less continental fluvial source similar to those reported by Dai et al. (2016) and Shangguan et al. (2020). The TiO2/Ni diagram also suggests acidic volcanic rocks and a few sedimentary rocks as sources (Floyd et al., 1989; Noori et al., 2016). The average CIW values for
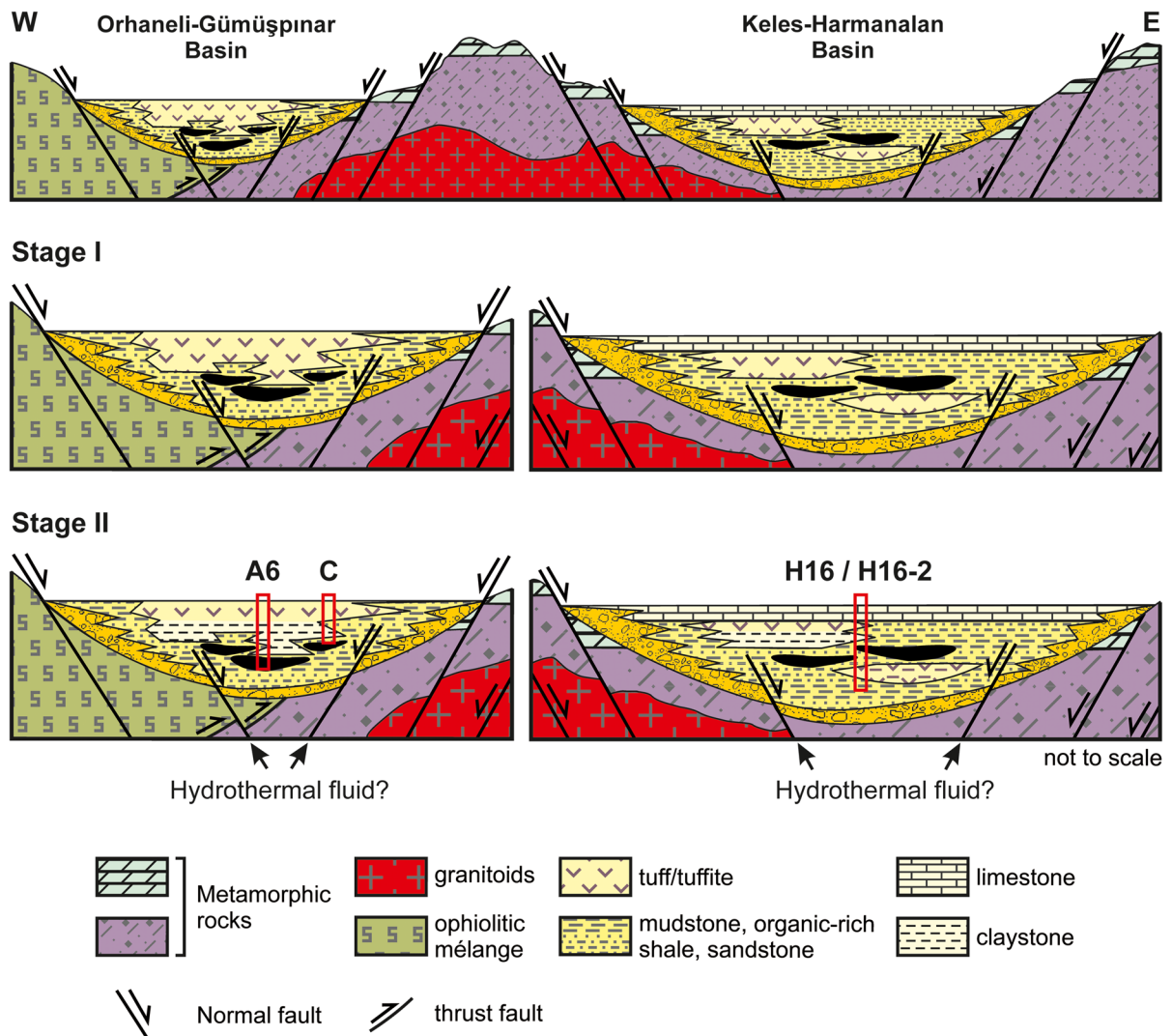
**Fig. 15** Simplified genetic model of the argillaceous fluvial-lacustrine sediments and volcanogenic material-intercalated coal seams in the Orhaneli-Gümüşpınar and Keles-Harmanalan basins

the argillaceous sediments in Orhaneli-Gümüşpınar (84.30) and Keles-Harmanalan (78.45) basins show a similar intensity of chemical weathering.

The authigenic smectite showed enrichment of $Al_2O_3$, $Fe_2O_3$, and MgO, and partial depletion of $SiO_2$, $Na_2O$, $K_2O$, and CaO relative to the rhyolitic to andesitic tuff/tuffite (Table 2; A6-25, C-17, C-20, and H16-7) in the Orhaneli-Gümüşpınar and Keles-Harmanalan basins similar to those reported for smectites from Manisa-Osmancalı, Turkey and Milos Island, Greece (Christidis & Dunham, 1993; Çiflikli et al., 2013). The positive correlation of $K_2O$ vs. Rb

suggests the replacement of K by Rb in feldspars, biotite, and illite during alteration of tuff/tuffite, argillaceous sediment, sandstone/mudstone, organic-rich shale, and marl (Motoki et al., 2015). The plots of $Al_2O_3$ vs. Zr and Th show similar immobile behavior during the alteration and indicate the presence of accessory zircon in the coal (Karayiğit et al., 2017). The positive correlation between $Al_2O_3$ and $TiO_2$ may be related to the abundant detrital material such as sandstone, mudstone, organic-rich shale, and argillaceous sediment inputs similar to those reported by Akinyemi et al. (2013). The positive correlation

between Nb and Y shows that the leaching of volcanic ash by groundwater was similar to that reported by Crowley et al. (1989).

The ratios of V/(V + Ni), Ni/Co, V/Cr, and Cu/Zn in both Orhaneli-Gümüşpınar and Keles-Harmanalan basins are indicative of paleoredox conditions (Table 2; Akinyemi et al., 2013; Hatch & Leventhal, 1992). These results are also consistent with the reported V/(V + Ni) ratios of < –0.46 and 0.54–0.82, V/Cr ratios of < –2 and > 2, Ni/Co ratios of < –5 and > –5, and a Cu/Zn ratio of < –1 indicate oxic, suboxic to anoxic conditions (Hallberg, 1976; Jones & Manning, 1994; Xiong et al., 2015). Furthermore, low U and high Th values are related to the devitrification of volcanic glass and alteration of feldspar and precipitation of montmorillonite in pyroclastic rocks during diagenesis (Zielinski, 1983).

The high concentrations of Ba (up to 3406 ppm), Sr (up to 8223.5 ppm), and Zr (up to 504.8 ppm) in the argillaceous sediments and tuff/tuffite exhibit alteration of volcanic ashes similar to those of the Franklin coal zone in Washington (USA) (Brownfield et al., 2005). The enrichment of Cr (up to 1197.4 ppm), Co (up to 60.5 ppm), and Ni (up to 548.2 ppm) in the sandstone and argillaceous sediments compared to the felsic tuff and organic-rich shale and carbonate (including marl) suggest a detrital contribution from the mafic–ultramafic source units in the study area similar to those reported by Zou et al. (2016) and Zhao et al. (2020). The enhancement of Cr, Co, and Ni values may suggest that these elements are associated with the Fe-bearing smectitic clay fraction and Fe-bearing sulfide via substitution of Fe by Cr, Co, and Ni in the octahedral site of smectite (Kadir et al., 2015).

The enrichment of LREE relative to HREE demonstrated a terrigenous or tuffaceous origin similar to those of the Permian and Jurassic coals, China (Shangguan et al., 2020). Enhancement of REE (max. 983.2 ppm) downward in the sequence of the deposit is related to the increase in smectitic clay fraction in the sediments (Fig. 13). Scott et al. (2015) and Li and Zhou (2020) reported that REE are accommodated mostly in the structures of smectites and kaolinite, in addition to adsorption by the clay fraction.

The positive Eu anomaly in acidic tuff may be related to the accumulation of feldspar released from the magma similar to that reported by Wolff et al. (2020). In addition, the positive Eu anomalies in shale and sandstone/mudstone may be related to the hydrothermal fluids at temperatures of > 200ºC contributing to the transformation from $Eu^{3+}$ to $Eu^{2+}$ under the reducing environment during the formation of the peat and an oxidized depositional environment, respectively (Dai et al., 2016; Jin et al., 2020; Mastalerz et al., 2020). The positive Ce anomaly in argillaceous sediments of the Keles-Harmanalan deposit indicates precipitation under an anoxic environment similar to argillites in the Huainan Coal Basin, China (Table 2 and Fig. 12; Chen et al., 2016), $Ce^{3+}$ is diluted along with the other REE from underlying organic matter, and $Ce^{3+}$ oxidized to $Ce^{4+}$ during in situ precipitation conditions (Taunton et al., 2000). The negative Ce anomaly in samples from the Orhaneli-Gümüşpınar deposit indicates leaching from argillaceous sediments by groundwater or hydrothermal fluid during post-depositional processes (Table 2 and Fig. 12; Chen et al., 2016).

### Stable isotope

The $\delta^{18}O$ and $\delta D$ values for the smectite and illite plot left of the supergene-hypogene line, close to the magmatic water box, suggesting the effect of hydrothermal activity during alteration (Sheppard & Gilg, 1996). The narrow $\delta^{18}O$ and $\delta D$ values reflect clay minerals' formed during hydrothermal alteration due to magmatic water mixing with surface water (Arslan et al., 2010). This suggestion is also supported by the occurrence of the Sadağ thermal spring-water located 6 km west of the Orhaneli-Gümüşpınar coal mines which have reservoir temperatures up to 119°C based on a silica geothermometer (Erkut, 2016) and the Orhaneli-Yapköydere hydrothermal Ni mineralization located 6 km north of the deposit (Örgün, 1993).

The low O-isotopic compositions of smectite (ranging from 1.39 to 5.09‰) from the mudstone and the organic-rich shale relative to the high values (range of 7.01–9.13‰) from the volcanic units suggest that the smectite has a detrital and authigenic origin. Similar low O-isotopic values of smectite (2.2–7.2‰) were also determined in siltstone and tuffite units from the Seyitömer coal deposit in western Anatolia (Erkoyun et al., 2017). The enrichment of the $\delta^{18}O$ value in volcanic units may be related to the authigenic formation of smectite by oxygen isotope exchange between the glass shards and water similar to what was reported by Cuadros et al. (1999).

The negative correlation of $\delta^{18}O$ with $Fe_2O_3$ in smectite indicates loss of Fe from the volcanic glass by increasing hydration resulting in the change of oxygen isotope composition during alteration (Compton et al., 1999). The depletion of $\delta D$ in clays shows that hydrogen isotope exchange with meteoric waters or fluid flow processes, post-formation, is associated with tectonism (Uysal, 2000).

The wide range of $\delta^{34}S$ values for pyrite and chalcopyrite in coal and tuff units of the Bursa-Orhaneli coal mines suggests that more than one phase of pyrite and chalcopyrite occurred during different phases of coalification under the effect of hydrothermal fluids similar to those reported by Lefticariu (2009). The similar wide range between negative to positive $\delta^{34}S$ isotope values of pyrite was also found in the fault gouge, siltstone, marl, and tonstein units from the Tunçbilek coal deposit (Erkoyun et al., 2019). Furthermore, the calculated formation temperature of 104.2–152.1°C for pyrite and chalcopyrite suggested a hydrothermal or magmatic contribution. The negative $\delta^{34}S$ values for pyrite and chalcopyrite show that kinetic fractionation between sulfate and sulfide is related to the high sulfate ratio supply downward compared with the bacterial sulfate reduction and formation of framboidal pyrite in the upper parts of coal sections (Smith & Batts, 1974). In contrast, positive $\delta^{34}S$ values of pyrite show that the ratio of bacterial sulfate reduction is greater than the ratio of downward sulfate supply toward the bottom of the coal sections in the Orhaneli-Gümüşpınar and Keles-Harmanalan deposits similar to those of the pyrite and chalcopyrite sulfur isotopes in siltstone and marl from the Seyitömer coal deposit (Erkoyun et al., 2017), the Garrick coal seam in Australia, and the Bakerstown coal bed, USA (Lyons et al., 1989).

## Conclusions

The detrital smectite input is accompanied by quartz, amphibole, and chlorite in fluvial and lacustrine sediments such as organic-rich shale, sandstone, and mudstone. On the other hand, the degradation of feldspar and devitrification of volcanic glass in tuff in the Orhaneli-Gümüşpınar and Keles-Harmanalan coal mines resulted in enrichment of Al, Fe, and Mg, and depletion of Si, all of which favored the formation of authigenic smectite under alkaline conditions via dissolution–precipitation mechanisms during diagenesis.

The development of smectite and smectite-edged illite as cement between detrital feldspar, amphibole, and quartz, and the close linkage between smectite flakes with resorbed feldspar and devitrified volcanic glass shards confirm the detrital and authigenic origin of smectite.

The presence of *Bisaccat pollen*, *Botryococcus braunii*, *Intratripollenites instructus*, *Inaperturopollenites hiatus*, and *Subtriporopollenites simplex* in organic-rich shale suggests a dry, warm to subtropical climate in fresh water and lakes in Late Eocene-Middle Miocene.

The average $Al_2O_3/TiO_2$ ratios and $TiO_2/Ni$ diagrams suggest acidic-intermediate and a few sedimentary rock sources. $SiO_2$ vs. $(Al_2O_3+K_2O+Na_2O)$ and $V/(V+Ni)$, $V/Cr$, $Ni/Co$, and $Cu/Zn$ ratios suggest arid–semiarid and oxic, suboxic to anoxic conditions.

The enrichment of LREE relative to HREE demonstrated a terrigenous or tuffaceous origin/provenance for the argillaceous sediments. The high $\Sigma REE$, positive Eu and positive/negative Ce anomalies suggest the fractional crystallization of feldspar and the contribution of hydrothermal fluids under a reducing environment. The $\delta^{18}O$ and $\delta D$ values of the smectite and illite fractions were formed during mixing of magmatic and surface waters.

The negative $\delta^{34}S$ values for pyrite and chalcopyrite imply the reduction of sulfate to sulfide by a hydrothermal or magmatic effect under a temperature range of 104.2–152.1°C. There is also bacterial reduction as shown by the occurrence of framboidal pyrite.

**Authors contributions** Hülya Erkoyun: Field studies, Determination of the analyzed data, Drafting of the manuscript.

Selahattin Kadir: Field studies, Determination of the analyzed data, Drafting of the manuscript.

Tacit Külah: Field studies, Determination of the analyzed data, Drafting of the manuscript.

⚙ Springer

**Data Availability** All data are available in the five Tables and 15 Figures included here.

**Code availability** Not applicable.

**Declarations**

**Conflicts of interest/Competing interests** The authors declare that there is no conflict of interest or competing interests.

**Ethics approval and consents to participate** Not applicable.

## References

Akinyemi, S. A., Adebayo, O. F., Ojo, O. A., Fadipe, O. A., & Gitari, W. M. (2013). Mineralogy and geochemical appraisal of paleo-redox indicators in Maastrichtian Outcrop shales of Mamu Formation, Anambra Basin, Nigeria. *Journal Natural Sciences Research, 3*, 48–64.

Aldega, L., Cuadros, J., Laurora, A., & Rossi, A. (2009). Weathering of phlogopite to beidellite in a karstic environment. *American Journal of Science, 309*, 689–710.

Arslan, M., Abdioğlu, E., & Kadir, S. (2010). Mineralogy, geochemistry and origin of bentonite in Upper Cretaceous pyroclastic units of the Tirebolu area, Giresun, Northeast Turkey. *Clays and Clay Minerals, 58*, 120–141.

Başol, B. (2009). *Büyükorhan granitoyidi kuzey kenarının petrografisi ve yan kayaçlarla ilişkisi (Orhaneli batısı, Bursa)* (p. 215). MSc thesis, İstanbul Univ., İstanbul.

Bau, M., & Dulski, P. (1996). Distribution of yttrium and rare–earth elements in the Penge and Kuruman Iron-Formations, Transvaal Supergroup, South Africa. *Precambrian Research, 79*, 37–55.

Bayraktar, C., & Altınay, A. (1985). *Balıkesir Bursa-Keles-Davutlar sahası sondajlı linyit aramaları* (p. 179). Mineral Research and Exploration of Turkey (MTA) Report No. 7780.

Benda, L., Innocenti, F., Mazzuoli, R., Radicati, F., & Steffens, P. (1974). Stratigraphic and radiometric data of the Neogene in northwest Turkey (Cenozoic and Lignites in Turkey). *Zeitschrift Der Deutschen Geologischen Gesellschaft, 125*, 183–193.

Bilgin, Y., Aksoy, D., & Dost, E. (1988). *Davutlar (Bursa-Keles) linyit sahası değerlendirme raporu* (pp. 145). Mineral Research and Exploration of Turkey (MTA) Report No. 8450.

Bohor, B. F., & Triplehorn, D. M. (1993). Tonsteins: Altered volcanic ash layers in coal-bearing sequences. *Geological Society of America, Special Paper, 285*, 1–44.

Brindley, G. W. (1980). Quatitative X-Ray mineral analyses of clays. In G. W. Brindley & G. Brown (Eds.), *Crystal Structures of Clay Minerals and their X-ray Identification* (pp. 411–438). Monograph 5, Mineralogical Society.

Brownfield, M. E., Affolter, R. H., Cathcart, J. D., Johnson, S. Y., Brownfield, I. K., & Rice, C. A. (2005). Geologic setting and characterization of coals and the modes of occurrence of selected elements from the Franklin coal zone, Puget Group, John Henry No. 1 mine, King County, Washington, USA. *International Journal of Coal Geology, 63*, 247–275.

Chen, B., Liu, G., Wu, D., & Sun, R. (2016). Comparative study on geochemical characterization of the Carboniferous aluminous argillites from the Huainan Coal Basin, China. *Turkish Journal of Earth Sciences, 25*, 274–287.

Christidis, G., & Dunham, A. C. (1993). Compositional variations in smectites: Part I. Alteration of intermediate volcanic rocks a case study from Milos Island, Greece. *Clay Minerals, 28*, 255–273.

Christidis, G., & Dunham, A. C. (1997). Compositional variations in smectites. Part II: Alteration of acidic precursors. A case study from Milos Island, Greece. *Clay Minerals, 32*, 253–270.

Clayton, R. N., & Mayeda, T. K. (1963). The use of bromine pentafluoride in the extraction of oxygen from oxides and silicates for isotopic analysis. *Geochimica et Cosmochimica Acta, 27*, 43–52.

Compton, J. S., Conrad, M. E., & Vennemann, T. W. (1999). Stable isotope evolution of volcanic ash layers during diagenesis of the Miocene Monterey Formation, California. *Clays and Clay Minerals, 47*, 84–95.

Craig, H. (1961). Isotopic variations in meteoric waters. *Science, 133*, 1702–1703.

Crowley, S. S., Stanton, R. W., & Ryer, T. A. (1989). The effects of volcanic ash on the maceral and chemical composition of the C coal bed, Emery Coal Field, Utah. *Organic Geochemistry, 14*, 315–331.

Cuadros, J., Caballero, E., Huertas, F. J., de Cisneros, J., & C., Huertas, F., & Linares, J. (1999). Experimental alteration of volcanic tuff: Smectite formation and effect on $^{18}O$ isotope composition. *Clays and Clay Minerals, 47*, 769–776.

Çelik, Y., Karayiğit, A. I., Oskay, R. G., Kayseri Özer, M. S., Christanis, K., Hower, J. C., & Querol, X. (2021). A multidisciplinary study and palaeoenvironmental interpretation of middle Miocene Keles lignite (Harmancık Basin, NW Turkey), with emphasis on syngenetic zeolite formation. *International Journal of Coal Geology, 237*, 1–33.

Çetin, A. (1985). *Harmancık-Kozluca (Bursa-Orhaneli) dolayının jeolojisi ve linyit olanakları* (p. 35). Mineral Research and Exploration of Turkey (MTA) Report No. 7660.

Çiflikli, M., Çiftçi, E., & Bayhan, H. (2013). Alteration of glassy volcanic rocks to Naand Ca-smectites in the Neogene basin of Manisa, western Anatolia, Turkey. *Clay Minerals, 48*, 513–527.

Dai, S., Graham, I. T., & Ward, C. R. (2016). A review of anomalous rare earth elements and yttrium in coal. *International Journal of Coal Geology, 159*, 82–95.

Durand, B., & Nicaise, G. (1980). Procedures for kerogen isolation. In B. Durand (Ed.), *Kerogen insoluble organic matter from sedimentary rocks* (pp. 35–53).

Ece, Ö. I., Ekinci, B., Schroeder, P. A., Crowe, D., & Esenli, F. (2013). Origin of kaolin-alunite deposits in Simav Graben, Turkey: Timing styles of hydrothermal mineralization. *Journal of Volcanology and Geothermal Research, 255*, 57–78.

Erkoyun, H., Kadir, S., Külah, T., & Huggett, J. (2017). Mineralogy, geochemistry and genesis of clays interlayered coal seams succession in the Neogene lacustrine Seyitömer coal deposit, Kütahya, western Turkey. *International Journal of Coal Geology, 172*, 112–133.

Erkoyun, H., Kadir, S., & Huggett, J. (2019). Occurrence and genesis of tonsteins in the Miocene lignite, Tunçbilek Basin, Kütahya, western Turkey. *International Journal of Coal Geology, 202*, 46–68.

Erkut, E. (2016). *Bursa Orhaneli bölgesi, Sadağ ve civarının hidrojeolojisi* (p. 120). MSc thesis, İstanbul Technical University, İstanbul.

Esenli, F., Kadir, S., & Ekinci Şans, B. (2019). Geochemistry of the zeolite-rich Miocene pyroclastic rocks from the Gördes, Demirci and Şaphane regions, west Anatolia, Turkey. *Geochemistry International, 57*, 1158–1172.

Floyd, P. A., Winchester, J. A., & Park, R. G. (1989). Geochemistry and tectonic setting of Lewisian clastic metasediments from the early Proterozoic Loch Maree Group of Gairloch, NW Scotland. *Precambrian Research, 45*, 203–214.

Güven, N. (1988). Smectites. In S. W. Bailey (Ed.), *Hydrous phyllosilicates* (Vol. 19, pp. 497–559). Mineralogical Society of America.

Hallberg, R. O. (1976). A geochemical method for investigation of palaeo-redox conditions in sediments. *Ambio Special Report, 4*, 139–147.

Harnois, L. (1988). The CIW index: A new Chemical Index of Weathering. *Sedimentary Geology, 55*, 319–322.

Hatch, J. R., & Leventhal, J. S. (1992). Relationship between inferred redox potential of the depositional environment and geochemistry of the Upper Pennsylvanian (Missourian) stark shale member of the Dennis Limestone, Wabaunsee County, Kansas, USA. *Sedimentary Geology, 99*, 65–82.

Hayba, D. O., Bethke, P. M., Heald, P., & Faley, N. K. (1985). Geologic, mineralogic and geochemical characteristics of volcanic-hosted epithermal precious-metal deposits. *Reviews in Economic Geology, 2*, 129–167.

Hosono, T., Lorphensriand, O., Onodera, S.-i, Okawa, H., Nakano, T., Yamanaka, T., Tsujimura, M., & Taniguchi, M. (2014). Different isotopic evolutionary trends of $\delta^{34}S$ and $\delta^{18}O$ compositions of dissolved sulfate in an aerobic deltaic aquifer system. *Applied Geochemistry, 46*, 30–42.

Hower, J., Eslinger, E. V., Hower, M. E., & Perry, E. A. (1976). Mechanism of burial metamorphism of argillaceous sediment: 1. Mineralogical and chemical evidence. *Geological Society of America Bulletin, 87*, 725–737.

Jiang, Y., Qian, H., & Zhou, G. (2016). Mineralogy and geochemistry of different morphological pyrite in late Permian coals. *South Chin. Arabian Journal of Geosciences, 9*, 1–18.

Jackson, M. L. (1956). *Soil chemical analysis – advanced course* (p. 894). Madison, Wisconsin, USA, published by the Author.

Jin, R., Feng, X., Teng, X., Nie, F., Cao, H., Hou, H., Liu, H., Miao, P., Zhao, H., Chen, L., Zhu, Q., & Zhou, X. (2020). Genesis of green sandstone/mudstone from Middle Jurassic Zhiluo Formation in the Dongsheng Uranium Orefield, Ordos Basin and its enlightenment for uranium mineralization, China. *Geology, 3*, 52–66.

Jones, B., & Manning, D. A. C. (1994). Comparison of geochemical indices used for the interpretation of paleo-redox conditions in ancient mudstones. *Chemical Geology, 111*, 111–129.

Kadir, S., Aydoğan, M. S., Elitok, Ö., & Helvacı, C. (2015). Composition and genesis of the nickel-chrome-bearing nontronite and montmorillonite in lateritized ultramafic

rocks in the Muratdağı region (Uşak, western Anatolia), Turkey. *Clays and Clay Minerals, 63*, 163–184.

Karayiğit, A. I., Littke, R., Querol, X., Jones, T., Oskay, R. G., & Christanis, K. (2017). The Miocene coal seams in the Soma Basin (W. Turkey): Insights from coal petrography, mineralogy and geochemistry. *International Journal of Coal Geology, 173*, 110–128.

Konak, A. (2002). *1/500.000 Scale Geological Map of Turkey, İzmir*. General Directorate of Mineral Research and Exploration of Turkey.

Kunze, G. W., & Dixon, J. B. (1986). Pretreatment for mineralogical analysis. In A. Klute (Ed.), *Methods of Soil Analysis, part 1. Physical and Mineralogical Methods* (2nd ed., pp. 91–100). American Society of Agronomy, Inc. and the Soil Science Society of America, Inc.

Lefticariu, L. (2009). *Intergrated study of mercury and trace elements distribution in Illinois coal* (p. 44). Final Report, Illinois Clean Coal Institute.

Leggo, P. J., Cocheme, J.-J., Demant, A., & Lee, W. T. (2001). The role of argillic alteration in the zeolitization of volcanic glass. *Mineralogical Magazine, 65*, 653–663.

Li, M. Y. H., & Zhou, M.-F. (2020). The role of clay minerals in formation of the regolith-hosted heavy rare earth element deposits. *American Mineralogist, 105*, 92–108.

Loges, A., Wagner, T., Barth, M., Bau, M., & Göb., S., & Markl, G. (2012). Negative Ce anomalies in Mn oxides: The role of $Ce^{+4}$ mobility during water-mineral interaction. *Geochimica et Cosmochimica Acta, 86*, 296–402.

Lyons, P. C., Whelan, J. F., & Dulong, F. T. (1989). Marine origin of pyritic sulfur in the Lower Bakerstown coal bed, Castleman coal field, Maryland (USA). *International Journal of Coal Geology, 12*, 329–348.

Mastalerz, M., Drobniak, A., Eble, C., Ames, P., & McLaughlin, P. (2020). Rare earth elements and yttrium in Pennsylvanian coals and shales in the eastern part of the Illinois Basin. *International Journal of Coal Geology, 231*, 1–20.

Moore, D. M., & Reynolds, R. C. (1989). *X-Ray Diffraction and the Identification and Analysis of Clay Minerals* (p. 332). Oxford University Press.

Motoki, A., Sichel, S. E., Vargas, T., Melo, D. P., & Motoki, K. F. (2015). Geochemical behavior trace elements during fractional crystallization and crustal assimilation of the felsic alkaline magmas of the state of Rio de Janeiro, Brazil. *Anais Da Academia Brasileira De Ciências, 87*, 1959–1979.

Nakoman, E. (1968). Contribution à l'étude de la microflore tertiaire des lignites de Seyitömer (Turquie). *Pollen Et Spores, 10*, 521–556.

Noori, B., Ghadimvand, N. K., Movahed, B., & Yousefpour, M. (2016). Provenance and tectonic setting of Late Lower Cretaceous (Albian) Kazhdumi Formation sandstones (SW Iran). *Open Journal of Geology, 6*, 721–739.

Ohmoto, H., & Rye, R. O. (1979). Isotopes of sulfur and carbon. In H. L. Barnes (Ed.), *Geochemistry of hydrothermal ore deposits* (pp. 509–567). New York.

Okay, A. I., Harris, N. B. W., & Kelley, S. P. (1998). Exhumation of blueschists along a Tethyan suture in northwest Turkey. *Tectonophysics, 285*, 275–299.

Okay, A. I., Nobble, P. J., & Tekin, U. K. (2011). Devonian radiolarian ribbon cherts from the Karakaya Complex,

NW Turkey: Implications for the Paleo-Tethyan evolution. *Comptes Rendus Palevol, 10*, 1–10.

Oskay, R. G., Bechtel, A., & Karayiğit, A. I. (2019). Mineralogy, petrography and organic geochemistry of Miocene coal seams in the Kınık coalfield (Soma Basin-Western Turkey): Insights into depositional environment and palaeovegetation. *International Journal of Coal Geology, 210*, 1–22.

Örgün, Y. (1993). *Topuk-Göynükbelen (Orhaneli-Bursa) yöresi Nikel oluşumlarının kökensel incelemes*i (p. 216). PhD thesis, İstanbul Technical Univ., İstanbul.

Özaksoy, V., Elmacı, H., Özalp, S., Kara, M., & Duman, T. Y. (2018). Holocene activity of the Orhaneli Fault based on palaoseismological data, Bursa, NW Anatolia. *Bulletin of the Mineral Research and Exploration, 156*, 1–16.

Reinink-Smith, L. M. (1990). Mineral asssemblages of volcanic and detrital partings in Tertiary coal beds, Kenai Peninsula, Alaska. *Clays and Clay Minerals, 38*, 97–108.

Rivas-Sanchez, M., Alva-Valdivia, L., Arenas-Alatorre, J., Urrutia-Fucugauchi, J., Ruiz-Sandoval, M., Roberts, F. I., & Loughnan, F. C. (1989). Mineralogy and economic significance of bentonite occurrences in the upper Hunter Valley. In *Proceedings of Mineralogy-Petrology Symposium, MINPET 89* (pp. 123–127). Australasian Institute of Mining and Metallurgy.

Roche, E., & Schuler, M. (1980). Étude palynologique du Complexe de Kallo. *S.G.B. Professional Paper, 178*, 13.

Sáez, A., Inglès, M., Cabrera, L., & de las Heras, A. (2003). Tectonic-palaeoenvironmental forcing of clay-mineral assemblages in nonmarine settings: The Oligocene-Miocene As Pontes Basin (Spain). *Sedimentary Geology, 159*, 305–324.

Sarıfakıoğlu, E., Özen, H., & Winchester, J. A. (2009). Petrogenesis of the Refahiye ophiolite and its tectonic significance for Neotethyan ophiolites along the İzmir-Ankara-Erzincan suture zone. *Turkish Journal of Earth Sciences, 18*, 187–207.

Scott, C., Deonarine, A., Kolker, A., Adams, M., & Holland, J. (2015). Size distribution of rare earth elements in coal ash. In *World of Coal Ash Conference, Nashville, TN*.

Selim, H. H., Tüysüz, O., & Barka, A. (2006). Güney Marmara bölümünün Neotektoniği (Neotectonics of the south Marmara sub-region). *İTÜ Dergisi, 5*, 151–160 (in Turkish with English abstract).

Senkayi, A. L., Ming, D. W., Dixon, J. B., & Hosner, L. R. (1987). Kaolinite, opal-CT, and clinoptilolite in altered tuffs interbedded with lignite in the Jackson Group, Texas. *Clays and Clay Minerals, 35*, 281–290.

Sezgül Kayseri, M., & Akgün, F. (2008). Palynostratigraphic, palaeovegetational and palaeoclimatic investigations on the Miocene deposits in central Anatolia (Çorum region and Sivas basin). *Turkish Journal of Earth Sciences, 17*, 361–403.

Shangguan, Y., Zhuang, X., Li, J., Li, B., Querol, X., Liu, B., Moreno, N., Yuan, W., Yang, G., & Pan, L. (2020). Geological controls on mineralogy and geochemistry of the Permian and Jurassic coals in the Shanbei Coalfield, Shaanxi Province, North China. *Minerals, 10*, 1–34.

Sheppard, S. M. F., Nielsen, R. L., & Taylor, H. P. (1969). Oxygen and hydrogen isotope ratios of clay minerals from porphry copper deposits. *Economic Geology, 64*, 755–777.

Sheppard, S. M. F. (1986). Characterization and isotopic variations in natural waters. In J. W. Valley, H. P. Taylor & J.

R. O'Neil (Eds.), *Stable isotopes in high temperature geological processes reviews in mineralogy* (pp. 141–162).

Sheppard, S. M. F., & Gilg, H. A. (1996). Stable isotope geochemisty of clay minerals. *Clay Minerals, 31*, 1–24.

Smith, J. W., & Batts, B. D. (1974). The distribution and isotopic composition of sulfur in coal. *Geochimica et Cosmochimica Acta, 38*, 121–133.

Suttner, L. J., & Dutta, P. K. (1986). Alluvial sandstone composition and paleoclimate, I. Framework mineralogy. *Journal of Sedimentary Research, 56*, 329–345.

Şengüler, İ. (2004). Güney Marmara Bölgesi kömürleri. *Jeoloji Mühendisliği Dergisi, 28*, 31–38.

Takagi, T., Koh, S. M., Song, M. S., Itoh, M., & Mogi, K. (2005). Geology and properties of the Kawasaki and Dobuyama bentonite deposits of Zao region in northeastern Japan. *Clay Minerals, 40*, 333–350.

Taunton, A. E., Welch, S. A., & Banfield, J. F. (2000). Microbial controls on phosphate and lantanide distributions during granite weathering and soil formation. *Chemical Geology, 169*, 71–382.

Taylor, S. R., & McLennan, S. M. (1985). *The continental crustal: Its composition and Evolution* (p. 312). Blakwell.

Tissot, B. P., & Welte, D. H. (1984). *Petroleum Formation and Occurrence*. Springer-Verlag.

Uysal, I. T. (2000). Clay-mineral authigenesis in the Late Permian coal measures, Bowen basin, Queensland, Australia. *Clays and Clay Minerals, 48*, 351–365.

Yiğitel, İ., Altınay, A., & Özcan, K. (1989). *Bursa-Keles-Davutlar kömür sahası jeoloji raporu* (p. 62). Mineral Research and Exploration of Turkey (MTA) Report No. 8767.

Yossifova, M. G., Dimitrova, D. A., & Ivanova, R. I. (2018). Mineral and chemical composition of some claystones from the Troyanovo-3 mine. *Maritsa East Lignite Basin, Bulgaria International Journal of Coal Geology, 196*, 93–105.

Wheeler, A., & Götz, A. E. (2017). Palynofacies as a tool for high-resolution palaeoenvironmental and palaeoclimatic reconstruction of Gondwana post-glacial coal deposits: No. 2 Coal Seam, Witbank Coalfield (South Africa). *Palaeobiodiversity and Palaeoenvironments, 97*, 259–271.

Whitney, D. L., & Evans, B. W. (2010). Abbreviations for names of rock-forming minerals. *American Mineralogist, 95*, 185–187.

Wolff, J. A., Forni, F., Ellis, B. S., & Szymanowski, D. (2020). Europium and barium enrichments in compositionally zoned felsic tuffs: A smoking gun for the origin of chemical and physical gradients by cumulate melting. *Earth and Planetary Science Letters, 540*, 1–12.

Xiong, J., Liu, X., & Liang, L. (2015). Experimental study on the pore structure characteristics of the Upper Ordovician Wufeng Formation shale in the southwest portion of the Sichuan Basin, China. *Journal of Natural Gas Science and Engineering, 22*, 530–539.

Zhao, L., Ward, C. R., French, D., & Graham, I. T. (2012). Mineralogy of the volcanic-influenced Great Northern coal seam in the Sydney Basin, Australia. *International Journal of Coal Geology, 113*, 94–110.

Zhao, L., Dai, S., Graham, I. T., & Wang, P. (2016). Clay mineralogy of coal-hosted Nb-Zr-REE-Ga mineralized beds from Late Permian strata, eastern Yunnan, SW China: Implications for paleotemperature and origin of the microquartz. *Minerals, 6*, 45.

Zhao, Q., Niu, Y., Xie, Z., Zhang, K., Zhou, J., & Arbuzov, S. I. (2020). Geochemical characteristics of elements in coal seams $4_1$ and $4_2$ of Heshan Coalfield, South China. *Energy Exploration & Exploitation, 38*, 137–157.

Zou, J., Tian, H., & Li, T. (2016). Geochemistry and Mineralogy of Tuff in Zhongliangshan Mine, Chongqing. *Southwestern China Minerals, 6*, 47.

Zielinski, R. A. (1983). The mobility of uranium and other elements during alteration of rhyolite ash to montmorillonite: A case study in the Troublesome Formation, Colarado, U.S.A. *Chemical Geology, 35*, 185–204.

🙎 Springer